CHARACTERISING FAILURE OF ARMOUR CERAMICS AT HIGH STRAIN RATE LOADING : EXPERIMENTS AND SIMULATIONS

M.Tech. Thesis

By

LEKHANA CHANDRAN

DEPARTMENT OF METALLURGY ENGINEERING AND MATERIALS SCIENCE

INDIAN INSTITUTE OF TECHNOLOGY INDORE

JUNE 2022

CHARACTERISING FAILURE OF ARMOUR CERAMICS AT HIGH STRAIN RATE LOADING : EXPERIMENTS AND SIMULATIONS

A THESIS

Submitted in partial fulfillment of the

requirements for the award of the degree

of

Master of Technology

by

LEKHANA CHANDRAN

DEPARTMENT OF METALLURGY ENGINEERING AND MATERIALS SCIENCE

INDIAN INSTITUTE OF TECHNOLOGY INDORE

JUNE 2022

INDIAN INSTITUTE OF TECHNOLOGY INDORE

CANDIDATE'S DECLARATION

I hereby certify that the work which is being presented in the thesis entitled **CHARACTERISING FAILURE OF ARMOUR CERAMICS AT HIGH STRAIN RATE LOADING: EXPERIMENTS AND SIMULATIONS** in the partial fulfillment of the requirements for the award of the degree of **MASTER OF TECHNOLOGY** and submitted in the **DEPARTMENT OF METALLURGY ENGINEERING AND MATERIALS SCIENCE, Indian Institute of Technology Indore**, is an authentic record of my own work carried out during the time period from August 2020 to June 2022 under the supervision of Dr. Eswara Prasad Korimilli, Assistant Professor, Department of Metallurgy Engineering and Materials Science, Indian Institute of Technology, Indore.

The matter presented in this thesis has not been submitted by me for the award of any other degree of this or any other institute.

08.06.2022

Signature of the student with date
(LEKHANA CHANDRAN)

This is to certify that the above statement made by the candidate is correct to the best of my knowledge.

08.06.2022

Signature of the Supervisor of M.Tech. thesis (with date)
(Dr. ESWARA PRASAD KORIMILLI)

LEKHANA CHANDRAN has successfully given her M.Tech. Oral Examination held on **2nd June 2022**.

Signature of Supervisor of M.Tech. thesis
(Dr. ESWARA PRASAD KORIMILLI)
Date: 08.06.2022

Convener, DPGC
(Dr. SUMANTA SAMAL)
Date:

Signature of PSPC Member #1
(Dr. HEMANT BORKAR)
Date: 09.06.2022

09-06-2022

Signature of PSPCMember #2
(Dr. INDRASEN SINGH)
Date: 09.06.2022

ACKNOWLEDGEMENTS

I would like to convey my sincere gratitude to my research supervisor Dr. Eswara Prasad Korimilli for the continuous guidance and encouragement he has given at all stages of this project. His way of problem solving and communicating conceptual knowledge has inspired me to look at research with a fresh perspective.

I also thank Dr. Ratna Kumar Annabatula, Associate Professor, Department of Mechanical Engineering, IIT Madras and his student Mr. Sri Datta for their valuable inputs and guidance in ABAQUS modelling and simulations.

I extend my deepest gratitude to Carborundum Universal Limited, especially to Dr. Santanu Mandal, Head – R&D, Industrial Ceramics Division, for providing the rb-SiC samples for the experimental study.

I could not have improved and gained more insights to the topic without the periodic assessment of my work and the suggestions put forward by my PSPC members, Dr. Hemant Borkar and Dr. Indrasen Singh. Thank you.

I am deeply indebted to Dr. Abhijit Ghosh for providing server access to carry on simulations and once again to Dr. Indrasen Singh, and everyone at Computer Aided Design lab for giving access to their computational resources. Thanks to Prof. Preeti A. Bhobe for providing the required machining facility.

I am extremely thankful to my colleagues Abhinav and Tulika, for mentoring and guiding us, let it be during experiments or during discussions and group meetings, which helped me learn a lot. A huge thanks to Sandeep for being there with me throughout this project, for inspiring me to work hard every day, and for all the good memories. I will forever be grateful to you all for making Mechanics of Materials Lab feel like home.

I take this opportunity to also thank Mr. Mayur Dhake and Mr. Shubham Verma for helping me in utilizing the instruments and facilities required for this project work.

Thanks to my friends and classmates, for my time here in IIT Indore.

Finally, thanks to my parents and family for their constant love and support.

DEDICATION

This thesis is dedicated to my parents
and sisters for their love,
encouragement and patience.

Abstract

Advanced ceramics used in armour applications are subjected to extreme loading conditions and hence understanding their failure under impact loading conditions helps in the development of materials with improved dynamic properties. Though the experimental techniques that characterize their strength and failure under impact loading conditions give a good estimate of failure strength, they fail to provide a comprehensive understanding of the failure mechanisms due to the limitations associated with the high speed imaging techniques. So, often the experiments are complemented by the finite element simulations to understand the failure processes. In the current study, the high strain rate behaviour (of modified Split-Hopkinson Pressure Bar tests) of extensively used armour ceramics such as Silicon Carbide, Boron Carbide, and Alumina are studied using finite element simulations in ABAQUS/Explicit. Initially efforts have been made to validate the numerical model and to understand the effect of varying experimental parameters and other properties on the deformation behaviour. Comparative study of the mechanical deformation behaviour of the different materials including stress distribution and damage evolution as well as estimation of their compressive strength and failure strains were done. Influence of geometry was also investigated. Finally, characterization and miniaturized-SHPB experiments were conducted on Reaction Bonded Silicon Carbide samples, with an attempt to correlate the microstructure and mechanical properties of the material with the dynamic results.

LIST OF PUBLICATIONS

- List of journal publications

    1. Lekhana Chandran, K. Eswara Prasad, Ratna K. Annabattula, Modelling the influence of SHPB parameters during high strain rate compression of silicon carbide (submitted to *Materials Today: Proceedings*, 2022)

- List of journal publications under commutation

    2. Lekhana Chandran, K. Eswara Prasad, Ratna K. Annabattula, Modelling the failure of advanced ceramics under high strain rate compression: A comparative study

- List of works presented in conferences

    1. Lekhana Chandran, K. Eswara Prasad, Ratna K. Annabattula, Modelling the failure of advanced ceramics under high strain rate compression, *International Conference on Advanced Materials and Mechanical Characterization (ICAMMC–2021)*, held in virtual mode, 2nd - 4th Decermber 2021 (Poster presentation)

- List of works accepted for upcoming conferences

    2. Lekhana Chandran, K. Eswara Prasad, Ratna K. Annabattula, Modelling the failure of advanced ceramics under high strain rate compression, *13th Symposium on Plasticity and Impact Mechanics (IMPLAST-2022)*, to be held in IIT Madras, 21st – 26th August 2022

    3. Lekhana Chandran, K. Eswara Prasad, Ratna K. Annabattula, Modelling the failure of advanced ceramics under high strain rate compression, *4th Structural Integrity Conference and Exhibition (SICE-2022)*, to be held in IIT Hyderabad, 12th – 13th, 14th – 16th December 2022

TABLE OF CONTENTS

LIST OF FIGURES

LIST OF TABLES

Chapter 1 :

INTRODUCTION

This chapter introduces the basic concepts required for the understanding of the work presented in this thesis. It starts with an overview of the current scenario in armour research which motivated us to carry out this study. The next section gives a brief description of armour ceramics which is the material under consideration followed by the functioning and science behind using them in armour applications. The fourth section discusses about the experiment used namely the SHPB technique, and finally why computational simulations of the same are necessary is explained in brief.

1.1. General overview

Defence and security are of utmost importance to the well-being and development of any country and enormous amounts of money is being spent to ensure national security and in enhancing their capabilities in preventing external threats. The military expenditure of regions across the world has consistently increased over time (Fig.1.1), with India being the third largest spender as per 2021 updates [1]. The budget allocated to the defence sector is always the highest in most nations and maximum share of India's 2022 budget is also for defence (percentage of total is marked in Fig.1.2), with an increase of about 10% from the previous year [2].

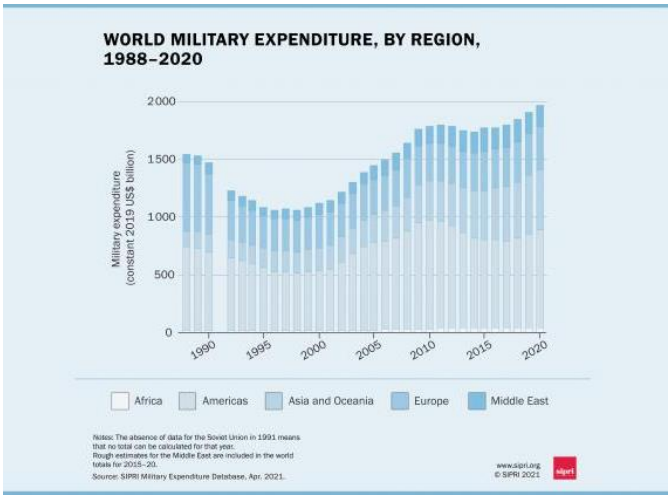

Figure 1.1: World military expenditure by region between the years 1988-2020 [1].

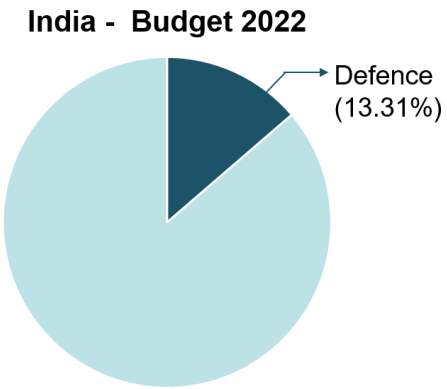

Figure 1.2: India's 2022 Union Budget allocation for defence.

The data throws light on the priority of developed and developing countries. The ever-evolving nature of weaponry and technology and rapid development of advanced materials call for immense research and development in army in a variety of fields like navigation and communication, transportation, weapons and equipment as well as armour material development.

Armor functions as a protective layer covering an object, person, or vehicle to deflect or distribute the destructive forces from threats like projectiles or bullets in such a degree that damage or injury is prevented. Historically metals were the preferred choice of material for manufacturing armour shields due to obvious reasons. But they were heavy and restricted movement of personnel and also increased the weight of bullet-proof vehicles and equipment. With time and technology, sophisticated projectiles and bullets came into the market and metals proved to be ineffective against them. Ceramics were first used as an armour during the Vietnam War of 1960s and their low density yet possession of superior properties like high hardness, high compressive strength, high melting temperature and good corrosion and wear resistance made them attractive in armor applications. The comparison between the ceramics alumina, boron carbide and silicon carbide with previously prevalent armour steel made in Fig.1.3 portrays why ceramics are employed in armours. As of today, ceramics plates are commonly inserted in bullet-proof vests for personnel protection and in vehicles and aircrafts, and works exceptionally good against small arms and very high impact threats.

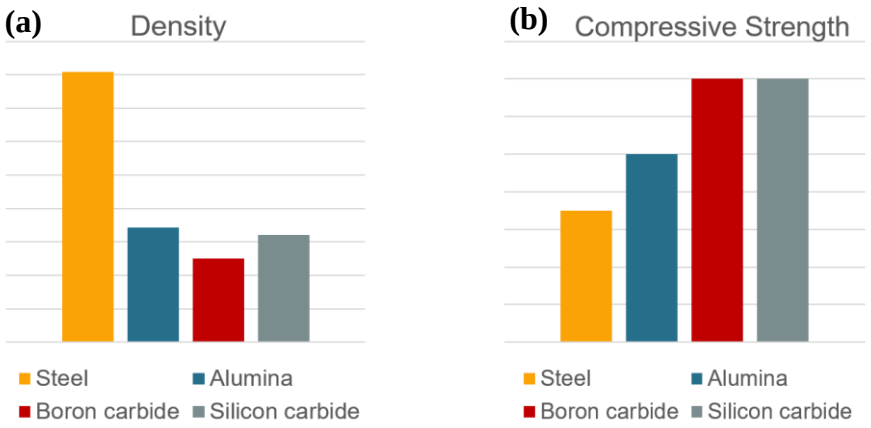

Figure 1.3: Comparison of **(a)** density, **(b)** compressive strength, of ceramics with steel.

1.2. Advanced ceramics

Ceramics are inorganic non-metallic oxides, nitrides or carbides having ionic or covalent bonds or a combination of both. Ceramics which are directly manufactured from natural sources are called classical ceramics and we are familiar with these in day-to-day applications. Armour applications require advanced ceramics which are manufactured under controlled conditions in order to impart excellent mechanical properties to the material. The processing parameters are regulated such that microstructure control occurs and there is reduction of defects and porosities within the material. Examples include silicon carbide, boron carbide, alumina and aluminium nitride.

1.2.1. Manufacturing methods

Advanced ceramics can be manufactured generally using the processing route in Fig.1.4. The starting material is processed powder of the base. Sintering is the coalescence of the powder particles forming a single solid particle with the edges of the particle becoming grain boundaries in the sintered material (illustrated in Fig.1.5). The remaining space might appear as pores within the solid. This particle is milled and used for the further manufacture of required ceramics using pressureless sintering, hot pressing or reaction bonding processes.

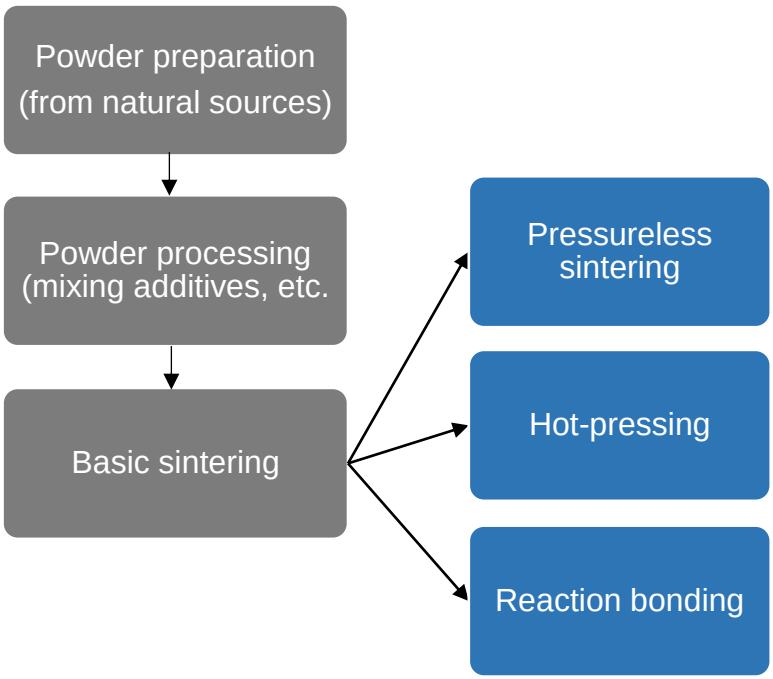

Figure 1.4: General processing route of advanced ceramics.

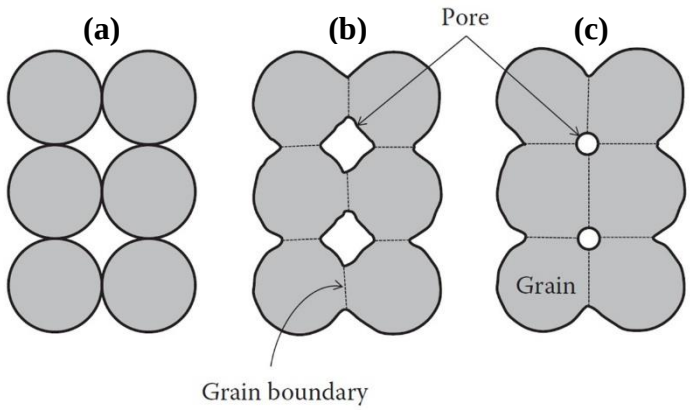

Figure 1.5: Sintering process showing **(a)** initial particles after compaction **(b)** coalescence of particles as sintering begins **(c)** sintered particles with pores [3].

Sintering as the next step is basically a densification process. The milled powder is sintered with additional sintering agents like graphite in order to reduce the sintering temperature. But final microstructure of the ceramic will therefore have graphite inclusions present. Most of the armour ceramics are processed through pressureless sintering or hot-pressing methods. Both processes are schematically shown in Fig.1.6. The former involves simple heating of the powder mixture in some suitable atmosphere. Microstructure and grain growth are controlled by proper control of temperature, pressure, composition and total sintering time. The latter is also a process similar to sintering, but the mixture is placed in a graphite mould and along with heat it is also compacted or pressed to achieve lesser porosity than simple sintering. This leads to a disadvantage of producing comparatively higher density ceramics [4].

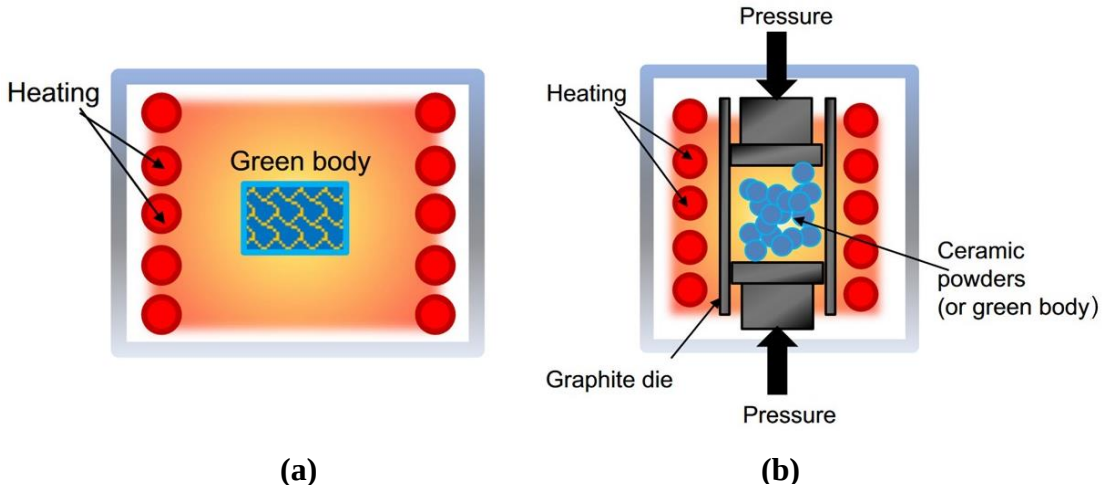

Figure 1.6: Densification of ceramics using **(a)** pressureless sintering **(b)** hot-pressing [4].

Reaction bonding or reaction sintering process has recently become prevalent in producing armour ceramics, especially silicon carbide. During the manufacture of reaction bonded silicon carbide (SiC), already existing powder of SiC is mixed with powdered carbon and an appropriate binding agent. This is infiltrated with molten or liquid silicon at high temperatures. The binding agent like phenolic resin is burnt off giving space for the flow of silicon, which chemically reacts with carbon to form new SiC. After complete reaction, a residual amount of silicon will be present in a matrix of original and new SiC [3, 4]. Ideally, no pores will be present in the final product and carbon is usually completely consumed, but imperfect flow of the liquid silicon can lead to patches of unreacted material in the manufactured product [5].

1.3. Ceramics as armour material

The extreme brittleness and low fracture toughness (a comparison with armour steel is made in Fig.1.7a and tensile strength of ceramics makes it impossible for them to be used as an independent armour material since it is bound to fracture after high velocity projectile impact. They are therefore used with a metallic backing layer. The ceramic layer acts as a disruptive layer which because of its high hardness (Fig.1.7b) it will push the projectile from entering the armour and further blunts and erodes the projectile itself. The kinetic energy of the incoming projectile is used up in the fracture and fragmentation of the ceramic because of creation of new surfaces. The impact pressure is distributed throughout the ceramic layer rather than confining to the point of contact. The backing layer is the energy absorbing material which provides bending stiffness to the structure and absorbs all the residual kinetic energy reaching it [3]. Fig.1.8a summarizes the concept of two-layer armours.

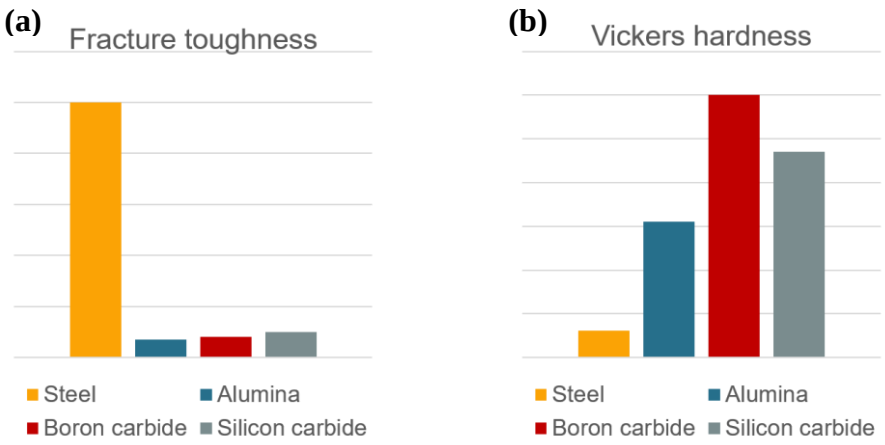

Figure 1.7: Comparison of **(a)** fracture toughness, **(b)** hardness, of ceramics with steel.

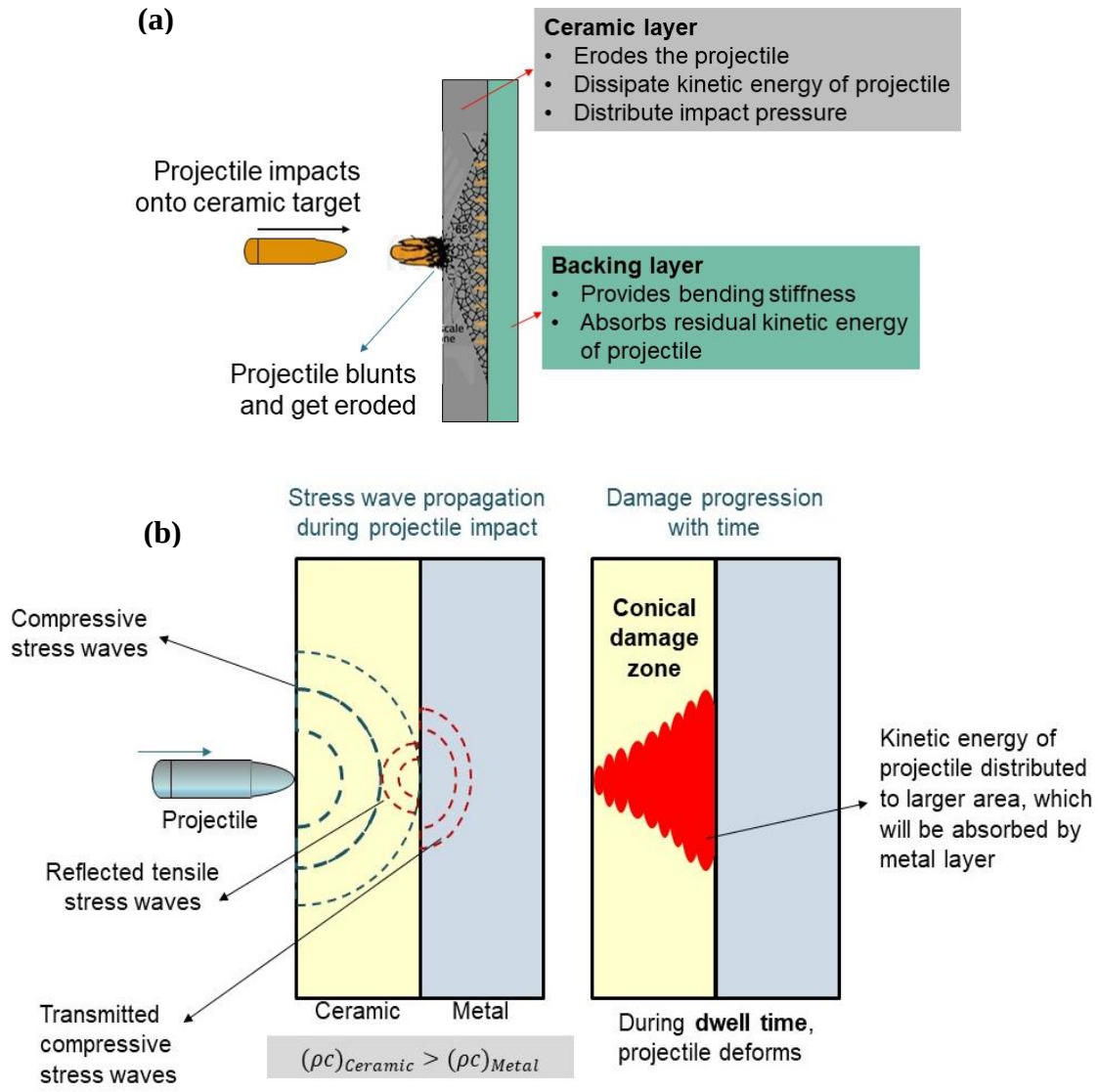

Figure 1.8: Schematic of projectile impact on ceramic armour with metallic backing layer showing **(a)** functions of each layer during projectile impact **(b)** stress wave propagation leading to fracture of ceramic armour structure.

The science behind projectile impact is explained graphically in Fig.1.8b in the following page. The metal backing layer is selected such that its mechanical impedance is lower than ceramics. The projectile impact generates compressive stress wave which propagates through the ceramic layer. The decrease in mechanical impedance from the ceramic to metallic layer lead to the reflection and transmission of tensile waves at the interface. Since ceramics have low tensile strength, damage and failure might begin at this interface once its strength limit exceeds. Once damage begins, there will be a difference in stressing at both sides of the ceramic plate and therefore this layer will bend, leading to even higher tensile stresses near the rear face. The backing layer is sufficiently stiff to prevent the entire

structure from failing under such conditions. With time, the damage area at the interface increases and it also progresses through the thickness of the ceramic, giving rise to a conical damage zone where a larger area is available to transfer energy to the metal backing plate for absorption. Damage emanating from the rear side of the ceramic and the front surface being intact prevents the projectile from penetrating the ceramic and cause any damage for a certain amount of time called dwell time and during this time the projectile will get deformed. If dwell time is sufficiently high and if projectile length is small, it might even completely shatter [6].

The conoidal fracture in ceramics is accompanied by formation of radial and circumferential cracks, as marked in Fig.1.9. Radial cracks originate from the point of impact and can rapidly propagate to the edges. Multiple crack formation at the impact point will lead to the formation of a tensile hoop stress which is relieved by radial cracking [7]. This is followed by development of a series of concentric circular cracks or circumferential cracking, which is due to the sudden pushing of the material right in front of the projectile, causing bending of the radial segments [4].

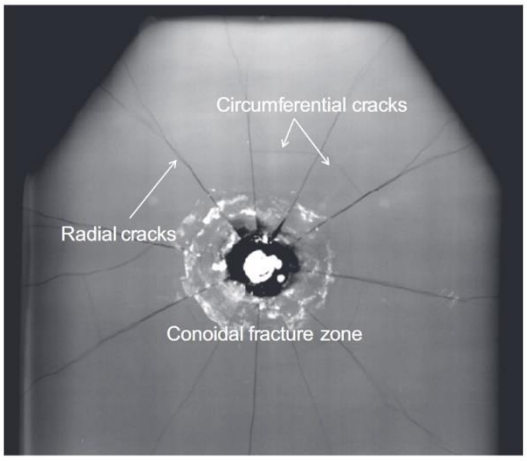

Figure 1.9: X-radiograph of impacted armour plate showing fracture zone and cracks [7].

The discussed fracture and cracking are essential for the effective distribution and absorption of incident kinetic energy and impact pressure, and thereby attain high level ballistic performance. They are all energy dissipation pathways for the material. But the the material should also not be over-cracked since this will not give sufficient strength to the armour during subsequent strikes. The flaws and porosity, grain boundaries, inclusions and phases might affect the required mode of failure and so mechanical and microstructural design play an important role [4].

1.4. Split-Hopkinson Pressure Bar technique

The preceding section demonstrates that during operation, armor ceramics are subjected to extreme loading conditions and hence, understanding their failure under impact helps develop materials with improved dynamic properties. Rate-dependent properties of materials are measured using a range of experiments according to the strain-rate regime under consideration [8] as compiled in Fig.1.10. Investigations at high strain rates are required to understand the dynamic behavior and ballistic properties of armor ceramics.

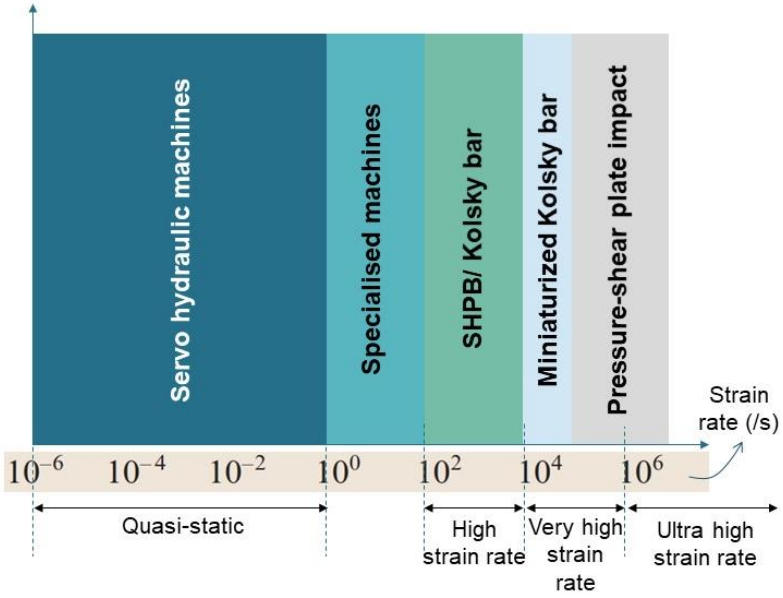

Figure 1.10: Experimental techniques to study deformation behavior of materials at different strain rate regimes.

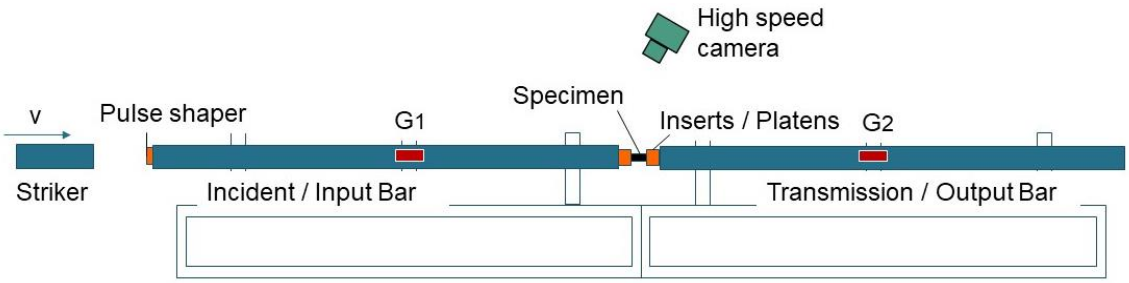

Figure 1.11: Schematic of modified-SHPB apparatus for ceramic testing.

Split Hopkinson Pressure Bar (SHPB) or Kolsky Bar technique is of focus in the current work (schematic of apparatus shown in Fig.1.11). It is extensively utilized to impart uniaxial compression to the specimen under study and thereby characterize its high strain rate (10^2

to 10^4 /s) mechanical properties. Compressive strength of the material plays a vital role during bullet impact and compression Kolsky bar experiments replicate similar scenarios.

Fundamentally, it involves determining the dynamic properties of materials using two long bars with the specimen placed between them [9]. The setup consists of an incident or input bar and a transmission or output bar between which the specimen under study should be placed. A striker bar impacts at one end of the incident bar, causing a compressive stress wave to propagate through the incident bar and further to the specimen. The bars are all made of the same material with high elastic modulus and so do not deform plastically. The specimen has lower mechanical impedance than the specimen and therefore a tensile wave is reflected at the input bar-specimen interface. The part of the compressive pulse which is transmitted to the specimen will again encounter impedance difference at the interface with output bar but since now wave propagation is from lower to higher impedance material, the reflected wave will be compressive in nature, and the remaining wave passes to the output bar. According to wave propagation theory [10], the reflecting wave will result in higher compressive stress. Similar reflection again repeats at the incident bar end of specimen, leading to multiple reverberations of compressive waves within the specimen and higher stress magnitude after each reflection. Finally, inelastic strain and plastic flow occurs in the specimen material when the stress is high enough, causing dynamic deformation and sometimes failure. The entire history of a stress wave passing through an SHPB setup is described as a wave propagation diagram in Fig.1.12.

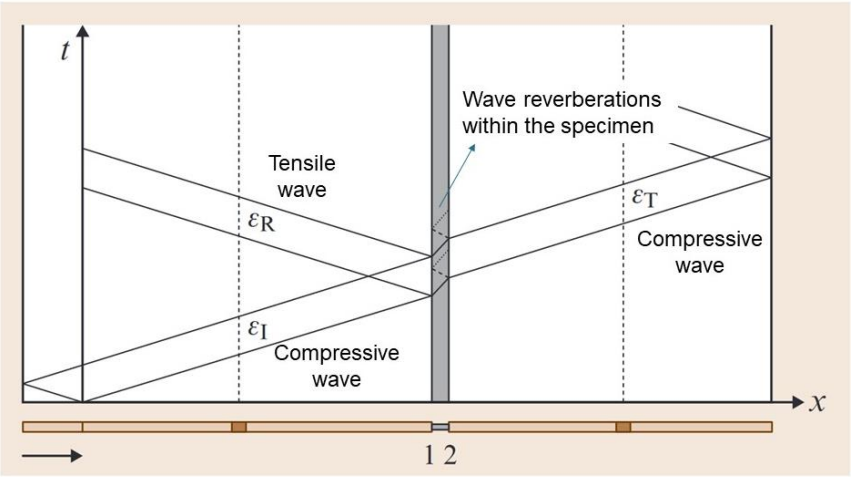

Figure 1.12: Wave propagation diagram showing the transmission and reflection of stress waves through Kolsky bars with respect to position and time [11].

Stress equilibration at both ends of the specimen and maintaining a constant strain-rate throughout deformation are necessary conditions to carry out valid SHPB experiments. For this enough number of reverberations of wave should happen within the specimen before its failure. Additionally, friction, dispersion and inertial effects should be negligible. Lubricants are generally used at specimen ends to reduce friction effects. Alignment between all bars and specimen should be ensured and any deviation might lead to additional wave reflection not caused by the specimen [11].

1.4.1. Modified-SHPB for ceramic specimens

Testing ceramics calls for a few modifications in the SHPB setup [12]. Ceramics are very hard and so the specimens might indent the bar ends during impact. The test sample is thus placed between even harder materials called platens/inserts, with area of cross-section generally higher than the specimen. Unlike the specimen, platen do not cause any damage to the bars since the area difference between the bars is less compared to that between specimen and bars, and so pressure is less since force is imparted to a larger area.

Moreover, ceramic specimens might fail before stress equilibrates at both ends of the specimen are due to its brittle nature and low failure strain values (<1%). This happens because enough number of reverberations do not occur within the specimen. Various methods [13–15] ensure that the rise time of the generated stress pulse increases and allows sufficient reverberations within the sample required to achieve dynamic stress equilibrium. The use of a thin disc of soft metal called pulse shaper between the striker and incident bar readily serves this purpose and is widely used in testing brittle materials like ceramics. It also leads to maintaining a constant strain rate for a longer duration and reduces radial wave dispersion in the bars. These two additional components are also depicted in Fig.1.11.

1.4.2. Mathematics involved in SHPB calculations

Calculation of the specimen's stress, strain, and strain rate during deformation is carried out using incident (ε_I), reflected (ε_R), and transmitted (ε_T) strain signals recorded by strain gauges mounted at the midpoint of both the incident and transmission bars (as depicted in Fig.1.11). Strain gauge G_1records ε_I and ε_R, G_1 records while ε_T. Oscilloscopes give amplified voltages corresponding to the signals (example shown in Fig.1.13) which is later processed to obtain each of the bar strain signals.

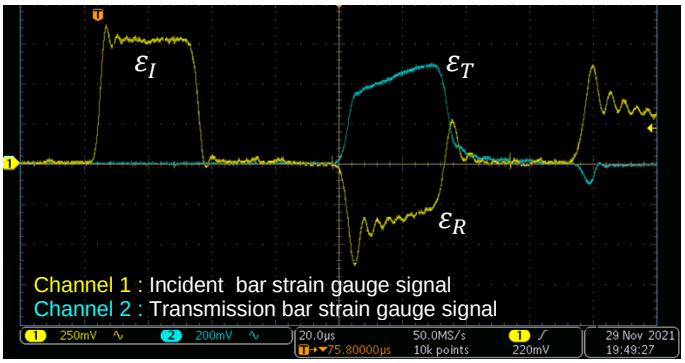

Figure 1.13: Oscilloscope signals obtained after SHPB experimentation.

The basic equations required based on the assumption that stress equilibration has occurred, are as follows [11] –

Specimen strain-rate : $$\dot{\varepsilon}_s(t) = -\frac{2c_b}{l_s}\varepsilon_R(t) \qquad (1.1a)$$

Specimen strain : $$\varepsilon_s(t) = \int_0^t \dot{\varepsilon}_s(\tau)d\tau \qquad (1.1b)$$

Specimen average stress : $$\sigma_s(t) = \frac{E_b A_b}{A_s}\varepsilon_T(t) \qquad (1.1c)$$

where, c_b = Bar wave speed

E_b = Elastic modulus of bar

A_b = Cross-sectional area of bar

A_s = Cross-sectional area of specimen

The strain rate is directly calculated from ε_R, with all other terms constant with time. So, the curve for strain rate vs. time will have a form same as that of reflected signal. The same is true for the specimen stress-time curve which will be similar to the transmitted signal.

During striker impact, kinetic energy is imparted to the bars and energy is dissipated due to each of the signals. The incident, reflected and transmitted energy respectively is calculated from the corresponding strain signals using the following equations [16] –

$$E_I = E_b A_b c_b \int_0^\tau \varepsilon_I^2(t)\, dt \qquad (1.2a)$$

$$E_R = E_b A_b c_b \int_0^\tau \varepsilon_R^2(t)\, dt \qquad (1.2b)$$

$$E_T = E_b A_b c_b \int_0^\tau \varepsilon_T^2(t)\, dt \qquad (1.2c)$$

As mentioned previously, it is necessary that stress at both ends of the specimen equilibrates for the SHPB test to be valid. The deviation from equilibrium is expressed using a factor R(t), which is a function of the stress at both ends of the specimen, calculated as [17] –

Stress at input bar end of specimen : $$\sigma_1 = E\frac{A_s}{A_b}(\varepsilon_i + \varepsilon_r) \qquad (1.3a)$$

Stress at input bar end of specimen : $$\sigma_2 = E\frac{A_s}{A_b}(\varepsilon_t) \qquad (1.3b)$$

$R(t)$ is the ratio of the stress difference between both specimen faces $(\Delta\sigma(t))$ and mean stress within the specimen $(\sigma_m(t))$. It is expressed as –

$$R(t) = \left|\frac{\Delta\sigma(t)}{\sigma_m(t)}\right| = 2\left|\frac{\sigma_1 - \sigma_2}{\sigma_1 + \sigma_2}\right| \qquad (1.4)$$

Equilibrium is said to have achieved when the factor is almost zero $(R(t) \leq 0.05)$.

1.4.3. Miniaturised-SHPB experiments

Very high strain rates cannot be achieved using conventional SHPB techniques. During compression in an SHPB, the specimen will obviously expand radially. But at very high strain rates inertia effects intensify and this restricts the sample's radial expansion. It was understood that smaller specimens should be used for achieving very high strain rates, but friction will be very high in such cases. Additionally, for small specimens the transmitted force will also be lower and it will be difficult to capture strain signals for the required calculations. This lead to the miniaturisation of the Kolsky bar setup, which will be able to achieve very high strain rates while retaining its ability to achieve attain lower strain rates. The use of smaller bars will reduce the dispersion of stress waves, there forth minimizing the inertial effects.

1.4.4. Pulse shaping effect

As mentioned in Section 1.4.1, it is essential to shape the incident signal produced during projectile impact while testing with ceramics. The effect of using a thin copper disc as pulse shaper has been studied using numerically modelled SHPB simulations (details of which are conscientiously described in Section 3.1.2), the results of which are given in Fig.1.14.

The obtained incident strain signals are shown in Fig.1.14a where the increase in rise time of the signal with the use of pulse shaper is clearly visible. Energy being utilized in the plastic deformation of the pulse shaper is the reason for the slow rise and slightly lower

magnitude of the signal. The reflected and transmitted signals given in Fig.1.14b gives an idea of the change in specimen strain-rate and stress respectively, because of the use of pulse shaper. The strain-rate plotted with respect to time in Fig.1.14c confirms that constant strain is maintained for a much longer time and the last graph of $R(t)$ factor (Fig.1.14d) depicts the shift from no equilibrium to very high level of equilibrium $(R(t)\sim 0)$ when the pulses were shaped.

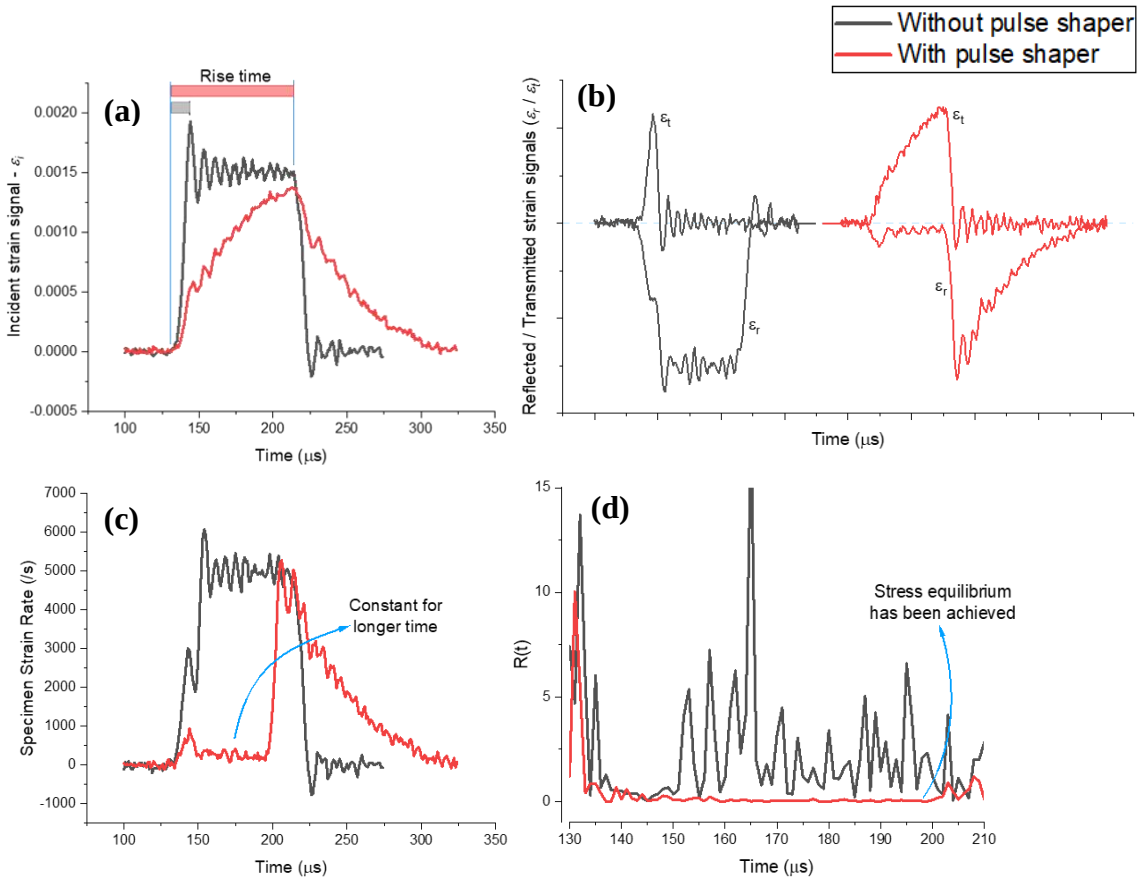

Figure 1.14: Simulated effects of employing a copper pulse shaper during SHPB experiment in **(a)** Incident bar strain signals **(b)** Transmitted bar strain signal **(c)** Specimen strain-rate **(d)** Deviation from equilibrium - $R(t)$.

1.5. Numerical modelling and simulations

The experiments which characterize materials at high strain rates are few, and the ones available are difficult to perform. Though these techniques, including SHPB, give good estimates of strength and failure, they do not provide a comprehensive understanding of the failure mechanisms due to the limitations associated with the high speed imaging techniques. Moreover, rigorous ballistic experimentations and trials are required before

incorporating armour ceramics for military use but they too expensive to conduct repeated destructive studies upon them. Thus they are often complemented with computer simulations with the help of numerical modeling to grasp the complete mechanical response and act as a tool to improve material design at reduced costs, if initial experimental data are available for material modelling and validation.

Numerical modeling required to aid simulating dynamic experiments has evolved tremendously in recent years. The mechanical response of materials can be described by equations of state (EOS) or through constitutive models. EOS are mostly determined by molecular-level modelling and calibration using experimental data. Constitutive models give a more efficient description under extreme conditions and they can be exercised at all integration/material points. They are classified as shown in Fig.1.15. Phenomenological models involve only curve-fitting without capturing the physics behind the problem but are commonly incorporated in finite element codes because they are computationally efficient [18]. Numerical models usually calculate the response of the material through huge number of iterations, where at each increment of time the change in strain causes corresponding change in stress as per the constitutive equations describing it [4].

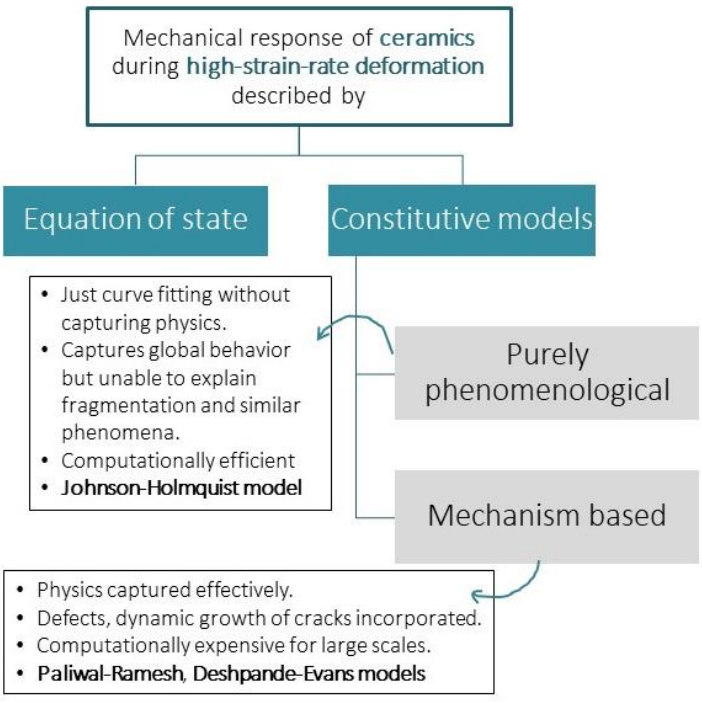

Figure 1.15: Classification and examples of ceramic constitutive models.

In practice, material constitutive models and EOS are implemented through codes like LS-DYNA, AUTODYN or user-written codes, using ANSYS, ABAQUS or similar packages.

Chapter 2 :

LITERATURE REVIEW AND OBJECTIVES

The past work that have been done in understanding the high strain-rate deformation behavior of armour ceramics, especially silicon carbide, has been summarized in this chapter. It comprises of experimental studies as well as computational research. The open questions in literature are highlighted, which forms the basis for framing the objectives of this work, as presented at the end of this chapter.

2.1. Kolsky bar studies on armour ceramics

Kolsky bar technique is the most commonly used experimental tool to investigate the dynamic strength and failure of armor ceramics. The results obtained from these studies [19–21] show that the compressive strength of the ceramics increases with increasing strain rate. The increase in strength at high strain rates is attributed to the inertial effects taking place in the dynamically propagating cracks as the number of flaws that gets activated increases with strain rate.

The dynamic behavior of the ceramic differs based on the processing method also. Lankford [19] compared the variation in compressive strength values with change in strain rates in hot-pressed Al_2O_3 and sintered SiC. It was observed that the former was weakly rate sensitive below a critical strain rate, while the latter was rate insensitive. But above critical strain rate, the strength rapidly increases in both cases. This kind of variation was also observed in hot-pressed SiC [20] and sintered SiC [22], where for the hot-pressed SiC macrocracking of the specimen happened only after peak stress was achieved but in sintered it occurred even before (see Fig.2.). The effect of manufacturing route was also studied by Pickup and Barker [23], which is also among the very few studies where damage behavior of reaction bonded silicon carbide was investigated..

Fragmentation analysis of the failed samples after quasi-static and dynamic compression was carried out by Wang and Ramesh [20] and it shows a wide distribution of fragments in the dynamic failed samples. This indicates that the wide distribution of flaws gets activated under dynamic loading conditions implying the importance of flaw size and distribution under dynamic loading conditions.

Shih et. al. observed polytypic transformation in SiC at high compressive stresses, and tried to attribute the increase in strength value to increase in 6H polytype within the material. Recently Prasad and Ramesh [24] with the help of nanoindentation experiments have shown that 6 layer hexagonal SiC polytype (6H-SiC) exhibits higher hardness (vis-v-vis strength) than the 4H-SiC polytype highlighting the role of polytype on the strength of the SiC. Thus it is necessary to understand the microstructural features coming into picture at dynamic loading conditions.

2.2. Computational studies of dynamic deformation tests

Even though experimental results with the help of high speed imaging techniques have led to understanding numerous aspects in ceramic deformation and failure like increase in strength with strain rate, axial splitting of specimens during SHPB deformation, and even modeling of fragmentation and fracture of ceramic materials, it is still difficult to investigate and study the internal crack propagation and damage. Computational studies help in this respect.

The ballistic performance of ceramics as target material has been extensively researched with the aid of modelling by Lundberg et. al. [25] and also recently by Khan et. al. [26] in order to understand alumina's fracture and fragmentation behavior. Similar work simulating both long rod [27] and spherical projectile [28] impact onto silicon carbide plates has been done and strong correlation with experimental observations validated the constitutive model used.

Very few researchers have numerically studied the SHPB deformation of ceramics, in spite of it being very effective in understanding the overall as well as internal response of specimen with time. Wang and Li [29] successfully replicated the axial splitting and deformation behavior of Al_2O_3 and Zhang et. al. [30] was able to capture difference in damage of SiC specimens at different strain-rates. Modelling of SHPB using cylindrical and cubical B_4C specimen by Venkatesan et. al. [31] gave insights about the specimen stress distribution which otherwise would have been impossible even with imaging techniques.

2.3. Research gaps and objectives

The open questions which needs to be addressed are highlighted in this section, followed by the proposed objectives of this work.

2.3.1. Research gaps

- Numerical modelling has enormous advantages when it comes to frame-by-frame understanding of rapid events like high strain rate experimentations. Very few authors have computationally simulated the SHPB deformation to get further understanding of ceramic's dynamic behavior. This will also help in selecting the experimental parameters without consuming any material since these tests are destructive in nature.
- Testing brittle materials essentially require the use of pulse shapers and control of other parameters. Even though studies to gain understanding of their influence on obtained results has been made, most of the work either concentrates only on the incident signals produced or are confined to ductile materials as specimen. Limited studies are available to investigate the effect of these parameters on ceramics.
- The Kolsky bar studies conducted hitherto report that the dynamic strength of SiC varies from 4-6 GPa and there are no reasons stated for this large variation in strength. Also, limited or no attention was paid in connecting the material parameters (such as grain size, composition, processing methods, texture, flaw size, nature of the polytypes etc.,) to the strength and failure.
- Even though most of the popular ceramics have already been dynamically testing, a comparison between their behaviors based on damage level and performance is yet to be carried out.
- Most of the published literature related to dynamic and ballistic studies on armour ceramics is from the USA, Europe, UK, and China and only a few studies are from India. Among them also in most of the cases material procurement is from oversees, making it expensive. It is necessary to conduct SHPB and other high strain rate experiments on indigenously produced advanced ceramics, so that it is possible to employ them in armour applications, and also control the processing parameters to design materials with superior dynamic properties.
- Studies on understanding the dynamic behavior of reaction bonded type SiC are almost none. Their popularity in armour applications is increasing, and it is necessary to understand its high-strain rate response and correlate with mechanical characteristics and microstructural features.

2.3.2. Objectives of this work

i. Computationally model and validate the SHPB experimental setup using Finite Element Modelling so as to simulate high strain rate deformation of armour ceramics.

ii. Investigate the influence of SHPB experimental parameters like impact velocity, striker length and pulse shaper dimensions on the results while testing ceramic specimens (silicon carbide is selected for this study).

iii. Compare the mechanical response of prevalent armour ceramics (silicon carbide, boron carbide, alumina) through the specimen-characteristic curves, stress contours, damage and element failure during high strain rate deformation imparted by the simulated SHPB test.

iv. Understand the dynamic deformation behavior of reaction bonded silicon carbide (rb-SiC) experimentally after mechanical and microstructural characterisation. Specifically focus on the dynamic stress-strain characteristics of the material and fracture mechanism involved.

Chapter 3 :

METHODOLOGY

All specifications pertaining to numerical and constitutive modelling required for conducting the Finite Element (FE) simulations are portrayed in this chapter. The focus then shifts towards the experimental methodology involved in carrying forward the analysis.

3.1. Computational framework

3.1.1. Material constitutive modelling

- *Johnson and Holmquist (JH-2) model*

The constitutive response of ceramic specimens is described using the modified Johnson-Holmquist (also referred to as JH-2) model [32] because of the ease and accuracy with which it can be implemented in finite element codes. It efficiently models damage in brittle materials at high strain-rates and pressures. The JH-2 parameters for SiC, B_4C and Al_2O_3 as well as a wide range of other ceramics are well established in literature and thus have been directly used in the present study.

The graphical description of the JH-2 model is presented in Fig.3.1. It consists of a strength model (Fig.3.1a) relating equivalent stress (σ) of intact and fractured (completely damaged) material, as well as partially damaged with pressure (P) and strain rate ($\dot{\varepsilon}$). Strength and pressure are normalized using corresponding Hugoniot Elastic Limit (HEL) components, thereby making most of the JH-2 parameters dimensionless and easy to estimate. T used in the equations is the maximum tensile hydrostatic pressure the material can withstand. A, B, C, M, and N are constants determined by experiments like plate-impact, diamond-anvil, Kolsky bar tests or sometimes quasi-static tests along with back-simulations if required [33].

D represents the damage accumulated in the material and is the ratio of plastic strain increment ($\Delta\varepsilon_p$) to plastic strain to fracture (ε_p^f). This transition from intact to fractured material is described by the damage model (Fig.3.1b), where D_1 and D_2 are the damage parameters.

A polynomial equation of state expressing pressure as a function of volumetric change (μ) forms the pressure model as shown in Fig. 3.c, where K_1, K_2 and K_3 are pressure constants. K_1 is the material's bulk modulus and K_2 and K_3 are determined by fitting pressure-volume

results. Pressure increment with damage is incorporated in the model as ΔP due to bulking of material and it is determined from energy considerations. Both the gradual damage phenomenon and incremental pressure with damage are improvements made to the previous JH-1 constitutive model, making JH-2 more accurate.

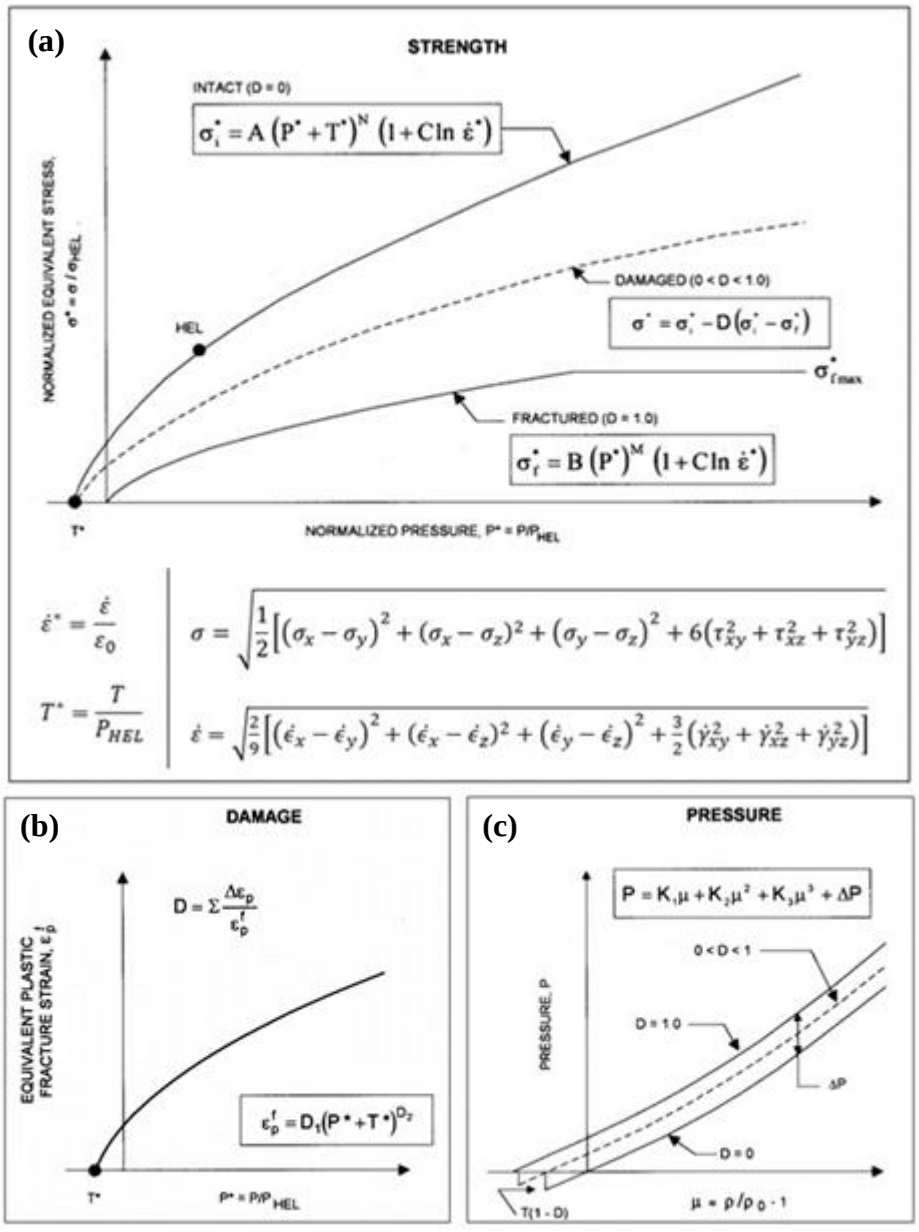

Figure 3.1: JH-2 ceramic model description for **(a)** Strength **(b)** Damage **(c)** Pressure.

- *Johnson and Cook (JC) model :*

The JC strength and failure model is employed to model the mechanical behavior of copper pulse shaper during high strain-rate impact. A thorough description of the strength model and determination of parameters are given elsewhere [34]. This includes material strength

parameters A, B, C, m and n, evaluated at or below transition temperature (T_0). The JC fracture model [35] include damage criterion T_0, expressed same as in JH-2 model. Failure strain constants D_1, D_2, D_3, D_4 and D_5 are required to calculate the plastic strain to failure, and these form the material damage parameters.

3.1.2. Numerical modelling

A series of numerical simulations are carried out to investigate the effect of experimental parameters on the mechanical response of the specimen. The dynamic behavior of commonly used armour ceramics is also compared, considering cylindrical and cubical geometries.

ABAQUS/Explicit software is used to create the computational framework of the modified-SHPB used to impart high strain-rate deformation to the selected specimen. SHPB experiments involve deformation at high speeds with relatively shorter response times, and there might be discontinuities in solution due to impact and material failure. Explicit dynamic analysis is ideal for such problems. For example, it allows incorporating material degradation and failure through the element deletion option, while the standard version does not [36]. It employs the explicit central-difference integration rule for calculations [37].

The model includes an assembly of striker, incident and transmission bars, a pair of inserts or platens, a cylindrical disc-shaped pulse shaper, and a specimen, together forming the modified-SHPB setup. The assembly along with part dimensions are illustrated in Fig.3.2.

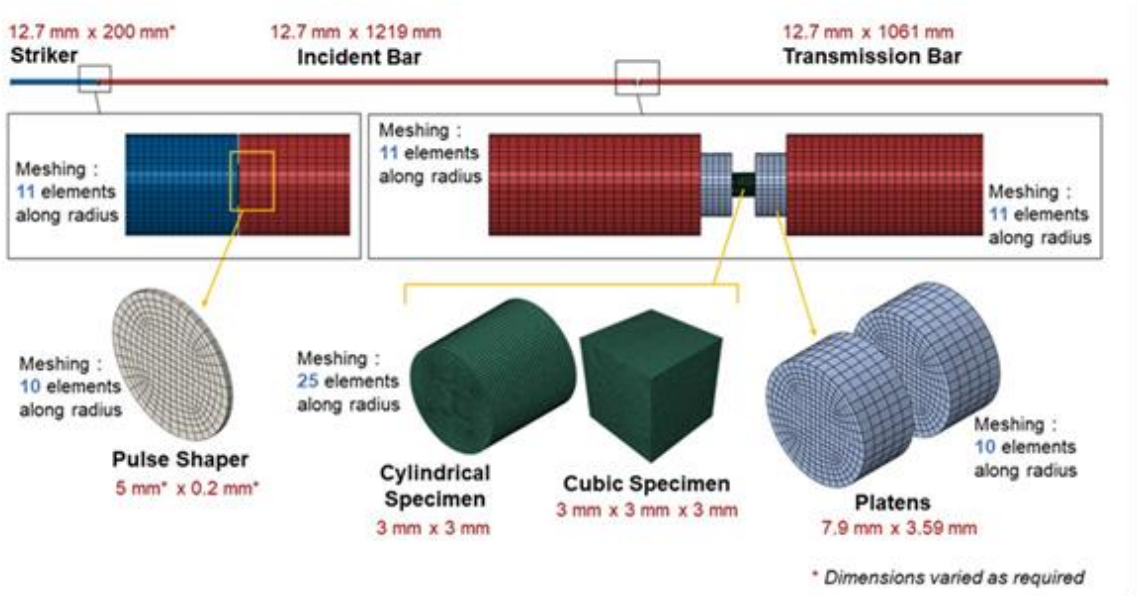

Figure 3.2: Assembly of SHPB setup including dimensions and mesh sizes of each part.

All parts are modelled as 3D deformable solids by extrusion. The incident and transmission bars are 1219 mm and 1061 mm long, respectively, with a diameter of 12.7 mm. The length of the striker bar is varied between 50 mm and 400 mm. Two different geometries of specimens, a Φ3 mm x 3 mm cylinder and a 3 mm x 3 mm x 3 mm cube were employed individually. The dimensions are selected based on Kolsky bar apparatus commonly used for experiments on ceramic samples [20, 21, 38, 39]. The platens used are Φ7.9 mm x 3.95 mm in size so that their impedance matches with the bars. Pulse shaper diameter and thickness are varied for the parametric study.

The bars are made of high-strength maraging steel, which remain elastic during the stress wave propagation, and tungsten carbide platens are used as inserts to prevent damage to the bar ends and also ensure one-dimensional wave propagation. The elastic properties required for the simulation of both the bars and insert material are given in Table 3.1 [20]. The mechanical response of the ceramic specimens under high strain rates, including damage, is described by the JH-2 constitutive model, available as a built-in user material in the ABAQUS/Explicit code which implements a VUMAT subroutine [40]. Silicon carbide (SiC), boron carbide (B_4C), and alumina (Al_2O_3) are the ceramic materials under study, and material change is reflected in the simulations by varying the JH-2 parameters (presented in Table 3.2), which various authors have experimentally and computationally determined ([41–43] for SiC, [31, 44] for B4C, [25, 45] for Al2O3). The pulse shaper is usually made of soft metals and its deformation and energy dissipation lead to a change in shape of the trapezoidal incident pulse to longer rise time triangular pulse. Copper pulse shaper is employed in the simulations, and JC strength and damage parameters (Table 3.3) are used to implement this [31, 34]. All tables are given at the end of this section.

Continuum three-dimensional eight-node linear hexahedral (brick) elements with reduced integration (C3D8R) are used to discretize the parts. In non-linear problems as considered here, full integration over-estimates the material's stiffness and gives results that do not precisely approximate real life. Reduced integration considers fewer Gaussian points and is a better option here. The computational time and effort are also reduced but with a slight loss of accuracy. Element controls are at default, and element deletion is enabled for the specimen to visualize damage. Mesh convergence study was carried out by varying the mesh size and comparing the specimen response and computational time. Fig.3.3 depicts the change in stress of the specimen with respect to time for different number of elements along the radius of each part. For the first three cases, simulations were carried out without a pulse

shaper, and it was later added to the assembly. It can be observed in Fig.3.3a that the specimen mesh size has a significant effect on the results as expected, and at least 25 radial elements (see inlet) are required in the specimen for convergence of results. According to Fig.3.3b, meshing inserts radially into 10 and more elements give repeating peak stress values. Though the mesh size of bars and pulse shaper does not cause much change in the response (Fig.3.3c,d), convergence is checked for accuracy, and it has been found that 11 and 10 elements along the radius are optimum for each respectively. The final mesh sizing is also mentioned in Fig.3.2 and a total of more or less 9,08,828 elements were produced.

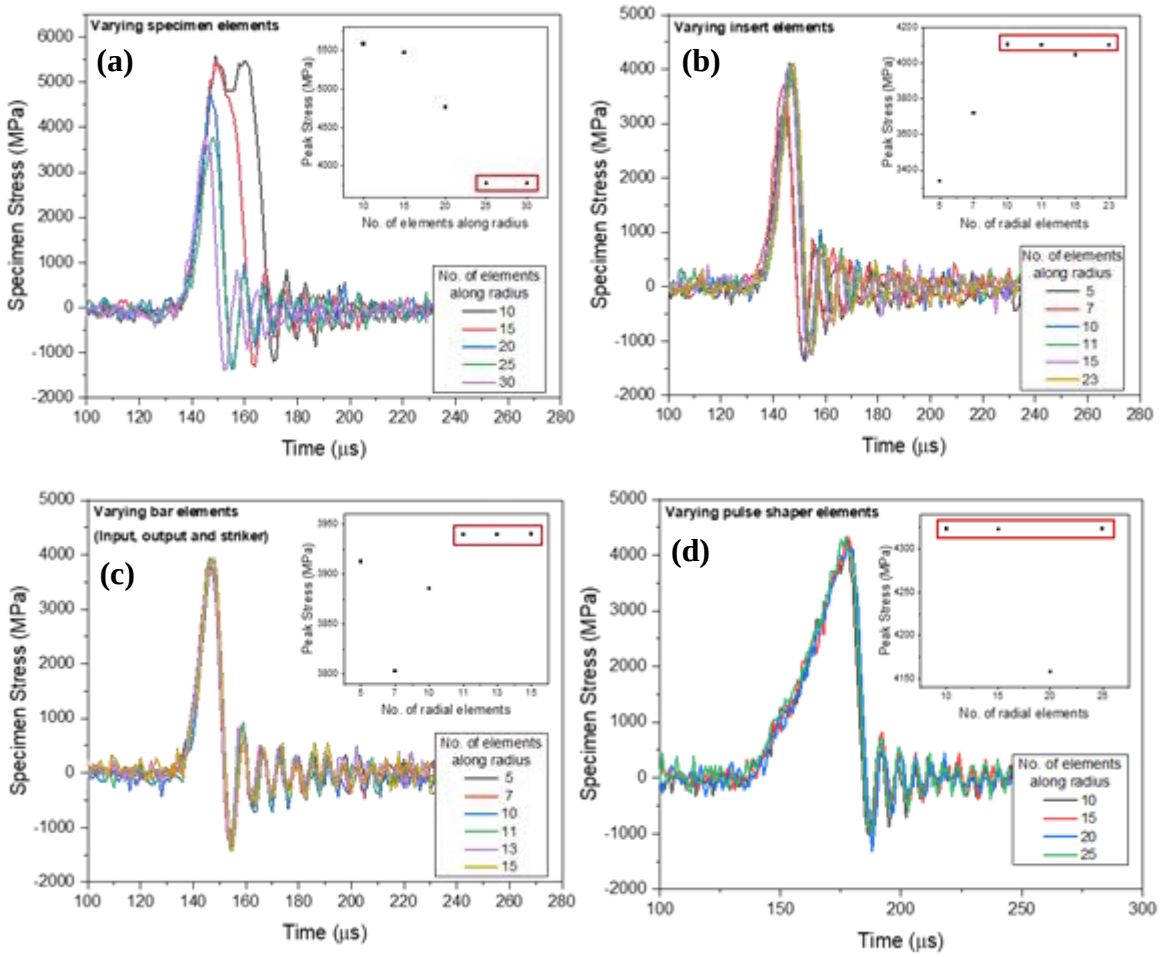

Figure 3.3: Specimen stress-time curves (along with peak stress achieved given in inlet) obtained by varying the mesh seeding along radius of **(a)** Specimen **(b)** Inserts / Platens **(c)** Bars **(d)** Pulse shaper.

The configuration is kept free without any boundary conditions. Different initial velocities between 10m/s and 20m/s are prescribed to the striker. General contact is adopted because it supports element-based surfaces which adapt to the exposed regions after deletion of

elements, and interactions between all surfaces except specimen surfaces are kept frictionless. Penalty friction formulation with friction coefficients varying from 0 to 0.1, but constant throughout the impact step of each run, is applied in the tangential direction at the specimen-insert interfaces to understand the effect of friction in the deformation behavior. In the normal direction, the default 'hard contact' pressure-overclosure relationship is selected. Contact is controlled using the nodal erosion option, which removes a node from the contact domain when all edges and faces associated with it erode.

The duration of the impact process is around 700μs. Field output requests are created for the entire assembly to visualize and quantify the stress wave propagation and also for the specimen alone for certain solution variables, including some solution-dependent state variables. History output requests for strain values are defined for elements at the midpoints of both input and output bars, which will act as strain gauges required to record the incident, reflected, and transmitted strain signals. Data is obtained for each microsecond.

Table 3.1: Properties of maraging steel and tungsten carbide for modeling bars and inserts of the SHPB setup [20].

			Maraging Steel (VascoMax C350)	**Tungsten Carbide (LC 403)**
Density	ρ	g/cm3	8.1	15.7
Young's modulus	E	GPa	200	690
Poisson's ratio	ν		0.29	0.22

Table 3.2: JH-2 parameters of selected ceramic materials to model specimen under study.

			SiC [41]–[43]	**B_4C** [31], [44]	**Al_2O_3** [25], [45]
Density	ρ	g/cm3	3.215	2.510	3.8
Bulk modulus	K	GPa	220	233	200
Shear modulus	G	GPa	193	197	135
Hugoniot elastic limit	HEL	GPa	11.7	19	5.9
Intact strength constant	A		0.96	0.927	0.989
Intact strength exponent	N		0.65	0.67	0.376
Strain rate constant	C		0.009	0.005	0
Fractured strength constant	B		0.35	0.7	0.77
Fractured strength exponent	M		1	0.85	1
Max. fracture strength ratio	σ^*_{max}		0.2	0.2	0.2
Hydro tensile limit	T	GPa	0.75	0.265	0.262
Damage constants	D1		0.02	0.001	0.01
	D2		1.85	0.5	1
	β		1	1	1

Table 3.3: JC parameters of copper pulse shaper used in the simulation [31, 34].

			OFHC Copper
Density	ρ	g/cm3	8.96
Bulk modulus	K	GPa	129
Shear modulus	G	GPa	46
Yield stress constant	A	GPa	0.2
Strain hardening constant	B	GPa	0.292
Strain hardening exponent	n		0.31
Viscous effect	C		0.025
Thermal softening constant	M		1.09
Reference strain rate	$\dot{\varepsilon}_o$		1
Melting temperature	T_{melt}	K	1356
Transition temperature	T_{melt}	K	295.14
Failure strain constants	D1		0.54
	D2		4.89
	D3		-3.03
	D4		0.014
	D5		1.120

3.2. Materials and Experiments

3.2.1. Materials

Hexagonal samples of rb-SiC (Reaction-bonded Silicon Carbide) received from Carborundum Universal Limited were used to study the mechanical, microstructural and dynamic properties (Fig. 3.4a). Silicon was infiltrated during the reaction bonding process at a temperature higher than 1600˚C. The dimensions of the as-received samples has been diagrammatically represented in Fig. 3.4b.

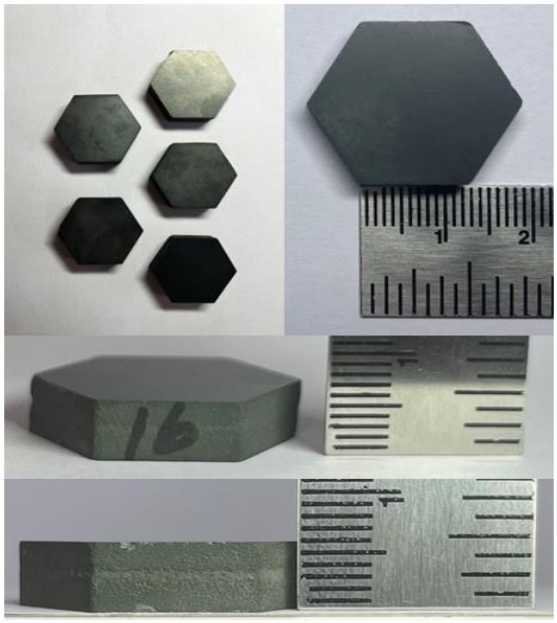

(a)

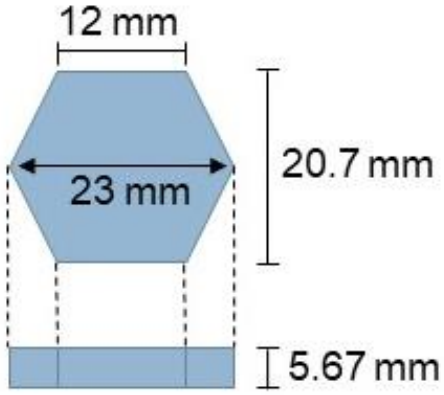

(b)

Figure 3.4: (a) As-received hexagonal rb-SiC samples **(b)** Schematic diagram representing sample dimensions.

The machining of the samples is challenging in nature. Due to high electrical resistivity of the sample, techniques like Wire-EDM which is commonly used in cutting conductive ceramics could not be employed here. Water jet cutting would be an ideal way to cut ceramics without introducing any machining induced damage, but due to non-availability of the facility, diamond cutting was employed for machining the samples.

A 5mm thick sample is machined using a low-speed diamond cutter along one of the hexagonal sides of the rb-SiC sample as depicted in Fig.3.5 for mechanical and microstructural characterisation. The required faces are grinded and polished using 150, 320, 400 and 600 grit size SiC papers, followed by 6µm, 3µm 1µm 0.25µm diamond pastes

on the polishing wheel. The sample is then ultrasonically cleaned in ethanol for 5 minutes to remove any residue.

Small specimens of the size 1 mm x 1 mm x 1.2 mm are cut for conducting high strain-rate experiments (diagrammatically shown in Fig.3.6). Long samples with cross-section 1.2 mm x 1 mm are machined out initially and then mounted onto an aluminium plate with the help of adhesive. 1mm cuts are made to get the final dimensions. Grinding and polishing could not be carried out due to extremely small sample size. They are then ultrasonicated.

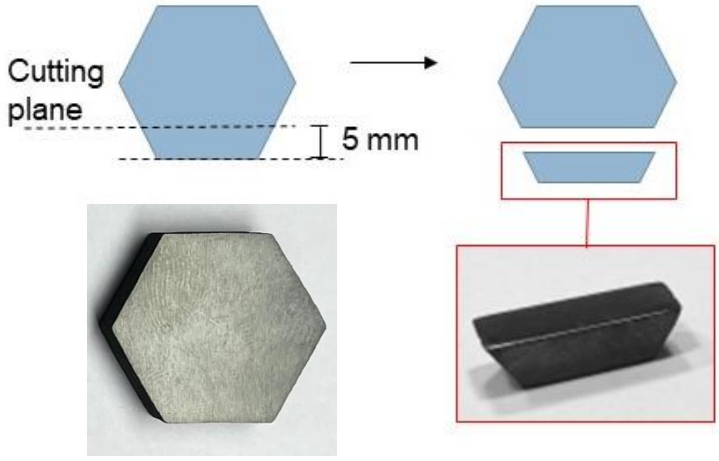

Figure 3.5: Sample machined for mechanical and microstructural characterisation studies.

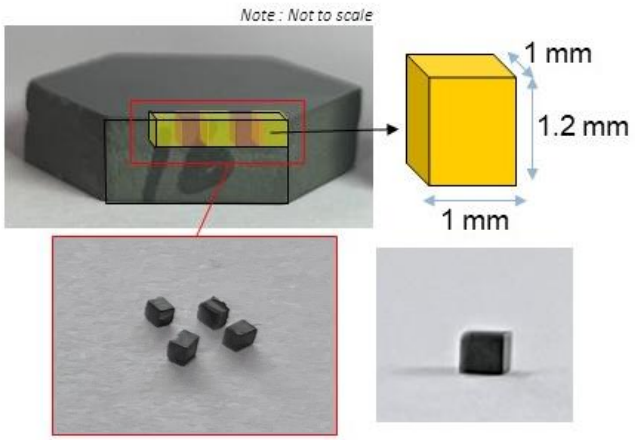

Figure 3.6: Sample machined to 1mm x 1mm x 1.2mm sizes for SHPB experiments.

3.2.2. Experiments

- *Microstructural characterisation*

Optical micrographs of the unetched polished inner as well as hexagonal faces of the sample machined as shown in Fig.3.5 are taken using ZEISS's Axio Vert. A1 Optical Microscope. Images of magnifications 5x, 10x, 20x and 50x were captured.

The material being a poor conductor of electricity, is gold coated and mounted on stubs using carbon tape while examining using Scanning Electron Microscope Supra55 Zeiss. Secondary electron mode at 15kV and 20kV are used to obtain a good contrast. Energy Dispersive Spectroscopy analysis was also undertaken on the same instrument.

- *Mechanical characterisation*

Microhardness testing is carried out on the sample machined as shown in Fig.3.5. Proper grinding and polishing ensures smooth finish and removal of scratches, aiding accurate measurement of indent sizes. A semi-automatic microhardness tester with Vickers and Knoop indenters is used to apply indentations on the inner face of the sample which is marked yellow in Fig.3.7a, for loads ranging from 1N to 20N. Experiments were carried out for lower loads of 0.25N and 0.5N too, but are not considered in the study due to formation of incoherent indents. Since Knoop indents are parallelogram-shaped where only the longer diagonal is crucial in hardness calculation, the technique helps in investigating material anisotropy by aligning the indent along and perpendicular to the sintering axis as Fig.3.7b depicts. All tests were performed by setting a dwell time of 10s at peak load and a loading-unloading velocity 60µm/s.

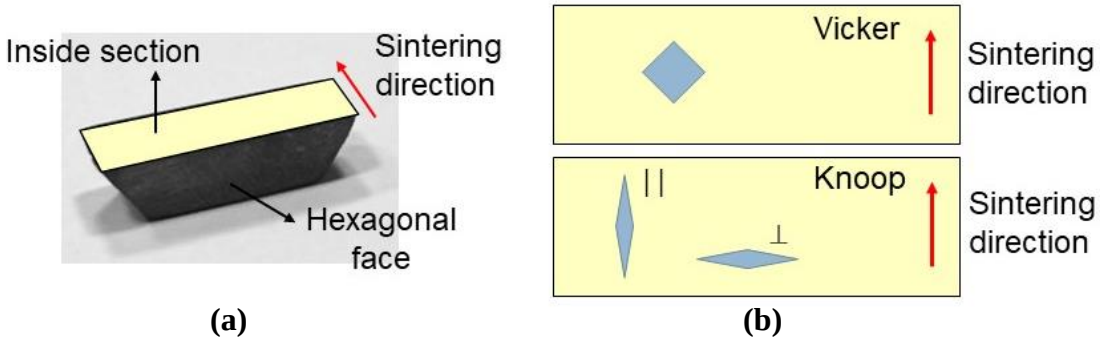

Figure 3.7: (a) Indentation surface of the demarcated in yellow **(b)** Vickers and Knoop indent orientation with respect to sintering direction.

- *Dynamic compression tests*

Miniaturised-SHPB apparatus is used to carry out high strain rate compression tests on 1mm x 1mm x 1.2mm cuboidal specimens of rb-SiC (Fig.3.6). The experimental setup along with all its components are given in Fig.3.8. It consists of 3 mm diameter maraging steel bars and uses a 60mm long striker for impact. Strain gauges are mounted onto the midpoints of the bars. The specimen is sandwiched between tungsten carbide platens using grease for hold and lubrication and loaded across the 1mm x 1mm cross section of the sample, i.e., along the sintered direction (see Fig.3.6 for reference). Beyond transmission bar a momentum trap is employed to damp the wave propagation after first loading. The small size of the bar and specimen make it more prone to misalignment and so before experimentation all parts should be aligned carefully. SHPB tests are done at 2 bar and 4 bar pressure (which will in turn change striker velocity), using Φ1mm copper pulse shaper of approximately 0.2 mm and 0.4 mm thicknesses respectively.

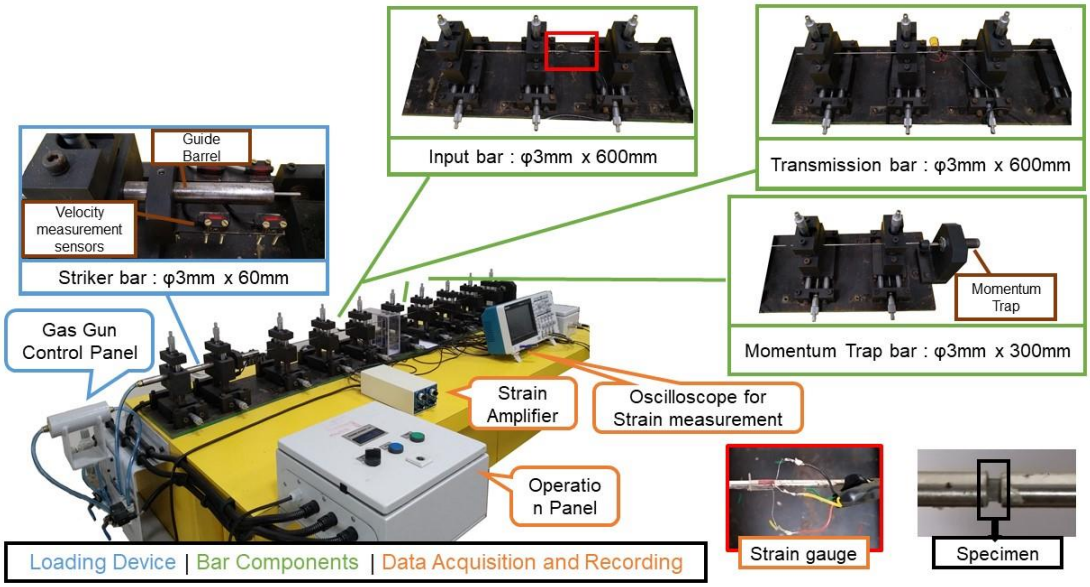

Figure 3.8: Miniaturised SHPB setup to conduct high strain-rate compression experiments.

Chapter 4 :

RESULTS AND DISCUSSION

The results section is divided into two – the first half focuses on the ABAQUS/Explicit computational results and the inference gained from it, and the next is about the experimental results. The chapter ends with a discussion on these obtained results.

4.1. Finite Element simulations

4.1.1. Model validation

The developed finite element (FE) model to simulate deformation at high strain rates using SHPB is validated in order to check its ability to replicate the experimental setup. Firstly, it should be ensured that there is no impedance mismatch between the platen and bar, which in turn can perturb the unidirectional wave propagation. For this, the model as elucidated in Section 3.1.2 is simulated, but without any specimen so as to look at the influence of platens alone. The strain signals obtained from the mid-points of both bars are of similar magnitude and shape as shown in Fig.4.1 and there is negligible reflected signal. This verifies that the stress wave generated is one-dimensional and the selected size of platens is accurate. Reflected signals obtained in all forthcoming results are solely due to the presence of specimen and can be used in calculating specimen characteristic curves. The specimen stress and strain rate achieved is on par with several SHPB results from literature.

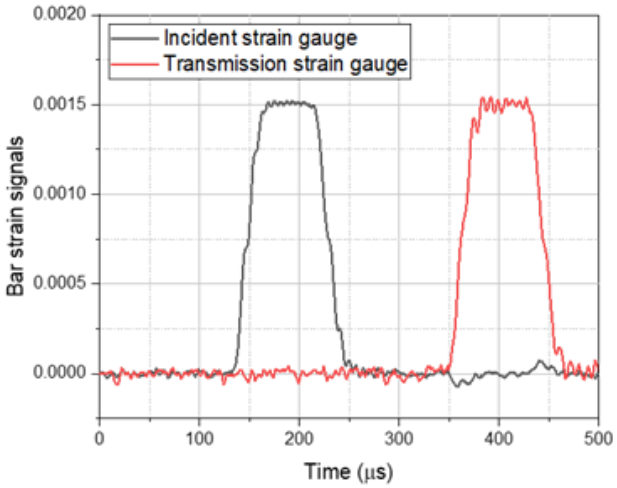

Figure 4.1: Bar strain signals from simulated SHPB experiment without specimen (Striker l = 200mm, v = 15m/s; Copper pulse shaper d = 5mm, t = 0.2mm).

4.1.2. Parametric study

SHPB experiments are controlled by controlling the incident waveform generated due to the striker impact. The influence of parameters like striker length and velocity as well as pulse shaper dimensions on the stress signal produced and also on ceramic deformation is thoroughly investigated.

- *Impact Velocity :*

Fig.4.4a shows the strain gauge signals obtained for each velocity. The magnitude of the strain signal produced in the incident bar due to impact of striker is expressed as [11] –

$$\varepsilon_I = \frac{v}{2c_b} \tag{4.1}$$

making it proportional to the impact velocity because the force imparted by striker increases and stress waves of higher magnitude are produced. The incident strain signals of the present study produced with the use of a pulse shaper, shown separately in Fig.4.4b, also displays this proportionality and shows a trend similar to the contact force produced at the incident bar end (Fig.4.2). In addition, the deformation of pulse shaper is also affected. The initial portion of the incident signals before inflection point represents the elastic deformation of the copper shaper and the region beyond until peak value is attained depicts its plastic deformation [46]. It is during the signal rise time (also marked in Fig.4.4b**)** that this plastic deformation occurs and it decreases with velocity, because the pulse shaper deforms rapidly at higher impact speeds.

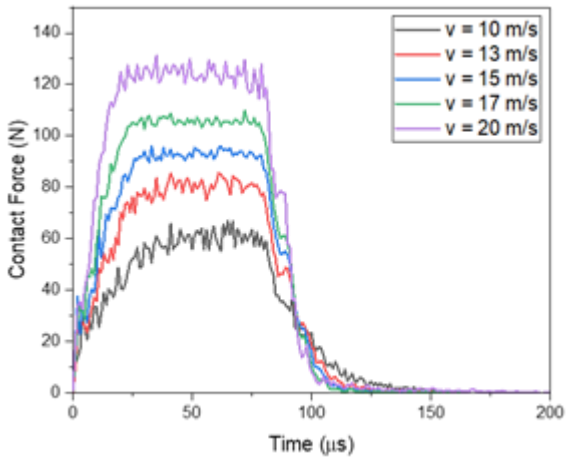

Figure 4.2: Contact force developed at incident bar end due to striker impact at different velocities.

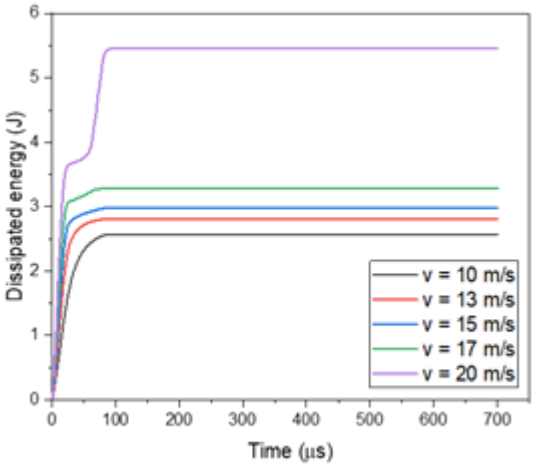

Figure 4.3: Energy dissipated during plastic deformation of pulse shaper at different striker velocities.

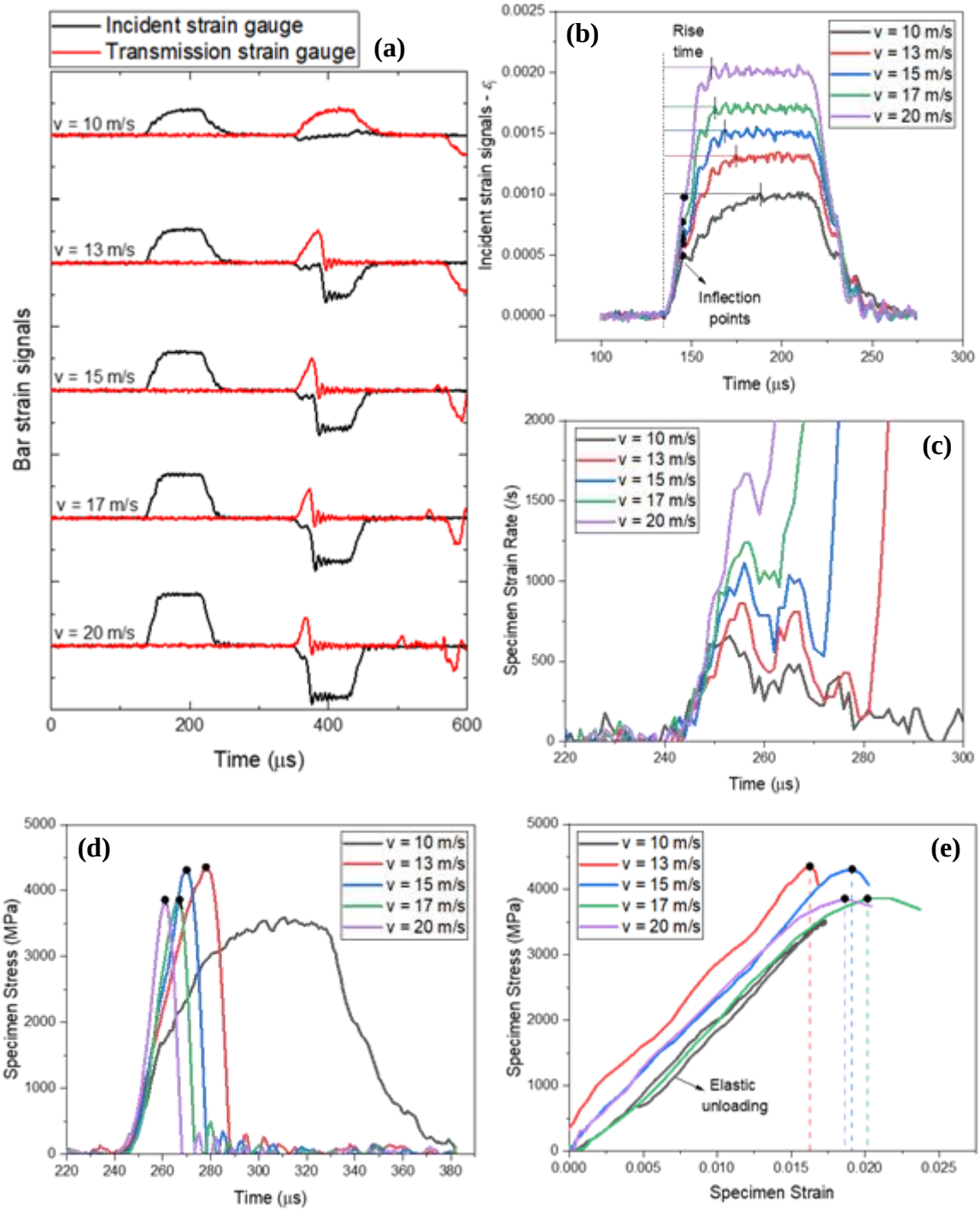

Figure 4.4: Effects of varying striker lengths on **(a)** Strain signals obtained at mid points of incident and transmission bars **(b)** Incident strain signals **(c)** Specimen strain-rate **(d)** Specimen stress **(e)** Specimen stress-strain curves (Striker v = 15m/s; Pulse shaper d = 5mm, t = 0.2mm).

Further insights about pulse shaper deformation can be gained by analyzing the energy dissipated during its plastic deformation, given by the equation [37, 47] –

$$\int_0^t \left(\int_V \sigma : \dot{\varepsilon}^p \, dV \right) d\tau \tag{4.2}$$

The linear increase in the curves shown in Fig.4.3 (previous page) depicts yielding of the copper shaper with strain hardening [48]. The observed strain hardening along with the increase in cross-sectional area increases its load carrying capacity, contributing to extended rise times. Plastic deformation uses and expels energy after macro and microstructural changes within the material and increase in the dissipated energy indicates higher plastic deformation of the material due to greater maximum stress. The increased slope at higher velocities signifies quicker achievement of peak signal values.

The strain rate achieved in the specimen increases with velocity as seen in Fig.4.4c, but it is not constant and reduces to zero before complete deformation for low impact velocities like 10m/s, and for high velocities of 20m/s the duration of constancy is less. The stress-time curves (Fig.4.4d) shows that deformation time reduces with an increase in velocity as expected, supporting the fact that the effect of pulse shaping reduces. It is to be noted that 10m/s shows a trend different from others with a deformation time much longer compared to ideal dynamic deformation curves. This deviation can be observed in the strain signals itself in Fig.4.4a where the reflected signal shifts from compressive to tensile. The stress-strain curve for the same contained in Fig.4.4e represents elastic unloading rather than failure observed at other velocities. Thus, even though the incident strain signal at this velocity indicates highest increase in rise time and thereby good pulse shaping, zero strain rate is achieved in the sample and it is only elastically deformed to negligible strains. Unlike other higher velocities, here the specimen remains intact even at the end of simulation time. 10m/s is therefore extremely low to cause any high strain rate response in the specimen for the current pulse shaper employed.

These results indicate that very high or very low velocities are not ideally preferred as constant strain rate throughout deformation is essential for valid SHPB experiments. Here, even a slight increase in velocity can give spurious results. The short range of acceptable striker velocities is not a general rule of hand, rather it is attributed to the selected combination of pulse shaper diameter and thickness. In order to obtain similar rise times

and ensure equilibrium at all velocities, the dimensions of shaper should also be varied proportionally, as discussed by Naghdabadi et. al [49].

- *Striker length :*

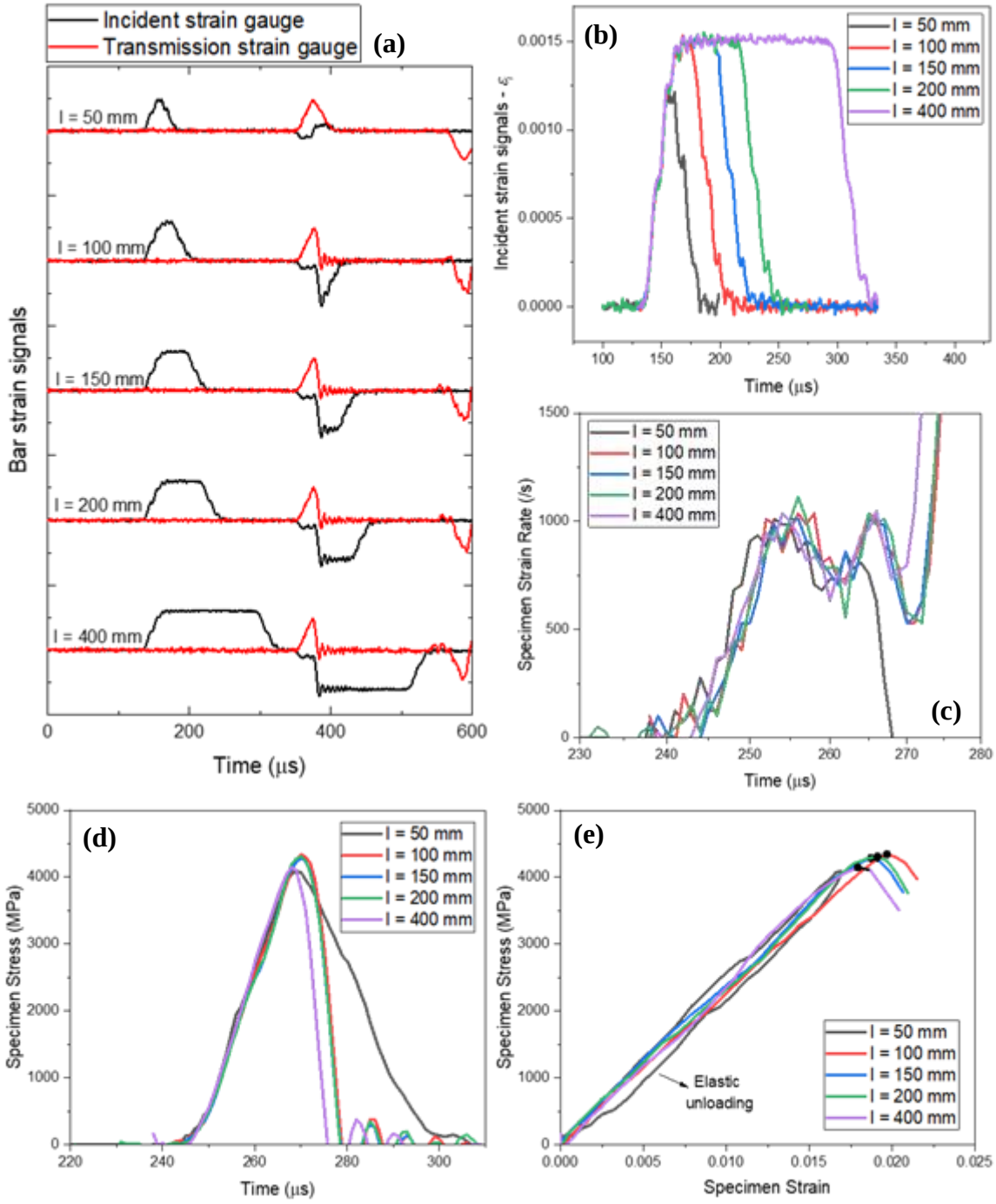

Figure 4.5: Effects of varying striker lengths on **(a)** Strain signals obtained at mid points of incident and transmission bars **(b)** Incident strain signals **(c)** Specimen strain-rate **(d)** Specimen stress **(e)** Specimen stress-strain curves (Striker v = 15m/s; Pulse shaper d = 5mm, t = 0.2mm).

Rather than magnitude of strain signals produced, it is the duration which will be affected by variation in striker bar length. The pulse duration can be written as –

$$\mathrm{t} = \frac{2 \times l_s}{c_b} \tag{4.3}$$

This implies that pulse duration increases with an increase of bar length, evidenced by Fig.4.5a and b. The magnitude of all cases remains the same because irrespective of length, the strikers all move with an equal velocity of 15m/s and impart the same force onto the incident bar. Only the time period of force application varies. As a result, the strain rate achieved in the specimen (Fig.4.5c) and its dynamic compressive strength observed from stress-time curves (Fig.4.5d) are equal for all lengths, the only exception being the case using 50mm striker bar.

Similar to the trends exhibited by very low velocity, the short striker of 50mm length also shows deformation behavior different from the rest. The shift from compressive to tensile nature of reflected signal is visible in Fig.4.5a and strain rate and strain of the specimen rapidly reduces to zero according to Fig.4.5c and e. Here too the specimen remains intact. Even though equilibrium has been achieved owing to the pulse length being longer than the specimen size, unloading occurs in the specimen before it plastically deforms because the force is applied for a very short time. All other striker lengths give valid results.

- *Pulse shaper diameter*

The incident strain signals for all pulse shaper diameters are of similar magnitude, showing a slight reduction with increase in d as seen in Fig.4.6. This is because more amount of the input kinetic energy is utilized in its plastic deformation, and only what remains appears as stress wave in the bar. This is also hinted by the plastic dissipated energy curves (Fig.4.7) showing a rise for larger diameters, which is obvious due to the larger volume of deformation involved. The magnitude of inflection points also marked in Fig.4.6 exhibits an opposite trend. Fig.4.8 gives the set of stress, strain rate as well as $R(t)$ values of the specimen with respect to time. It is observed that the strain rates are alike, giving rise to almost same compressive strength values. Initially, the stress in the specimen is comparatively lower for the 4mm diameter case, with a sudden increase in slope, while the 6mm pulse shaper gives rise to higher stress at the beginning continued by slower increase. The deformation time is akin for all diameters. The deviation from equilibrium, plotted

along the top x-axis shows that equilibrium is achieved in all cases during deformation. Higher the diameter, stresses in the specimen get equilibrated comparatively faster.

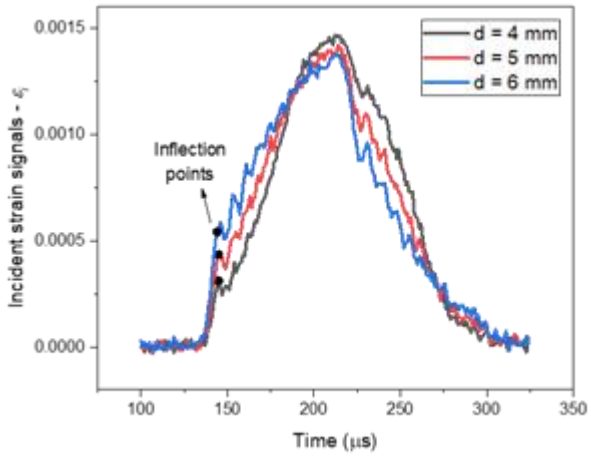

Figure 4.6: Effect of varying pulse shaper diameters on incident strain signals (Striker l = 200 mm, v = 15 m/s; Pulse shaper t = 0.2 mm).

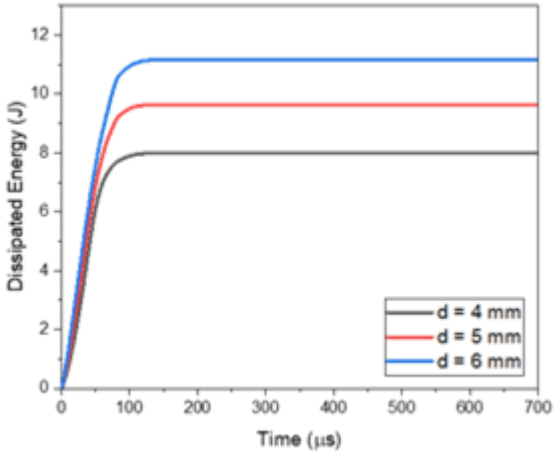

Figure 4.7: Energy dissipated during plastic deformation of different diameter pulse shapers.

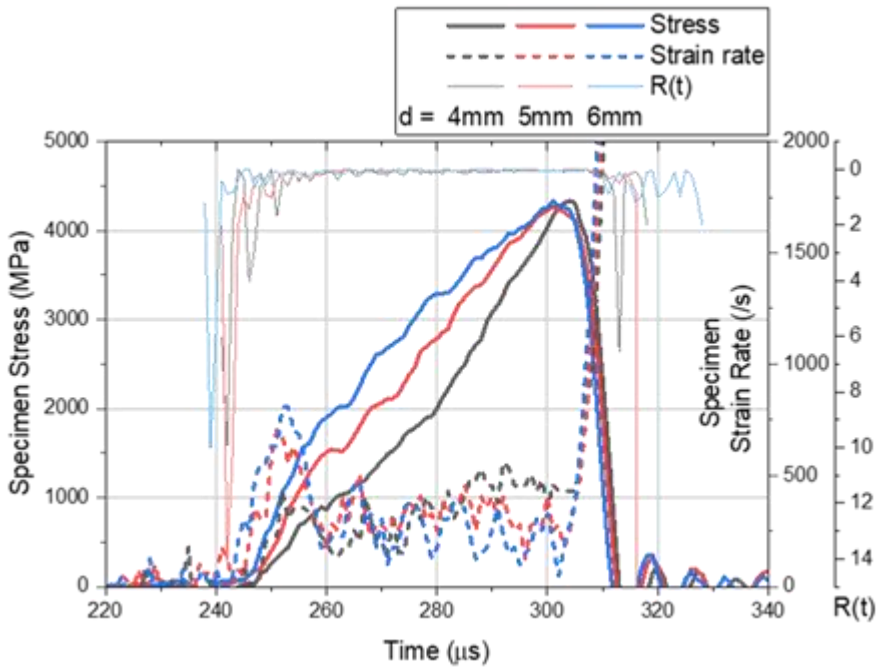

Figure 4.8: Stress, strain rate and $R(t)$ curves of specimen with respect to time when pulse shapers of varying diameters are used.

- *Pulse shaper thickness*

A reduction in the magnitude of incident strain signals can be observed in Fig.4.9a (next page), with a corresponding decrease in the inflection points too. The reason is same as the previous case of varying diameters. This is reflected as increase in the dissipated energy during plastic deformation plotted in Fig.4.9d. The signals also show increase in rise time and longer pulse duration as thickness increases. The strain rate values (Fig.4.9b) reduce slightly with thickness increase, which can be attributed to the incident signal magnitudes. The peak stress values (Fig.4.9c) increase slightly with considerable increase in the total deformation time, and constant strain rate is maintained throughout the deformation in all three cases individually given in Fig.4.10 (also given in next page). Each of the $R(t)$ curves illustrate that equilibrium is achieved for all thicknesses at the same time and it is maintained for a longer duration when thickness is larger.

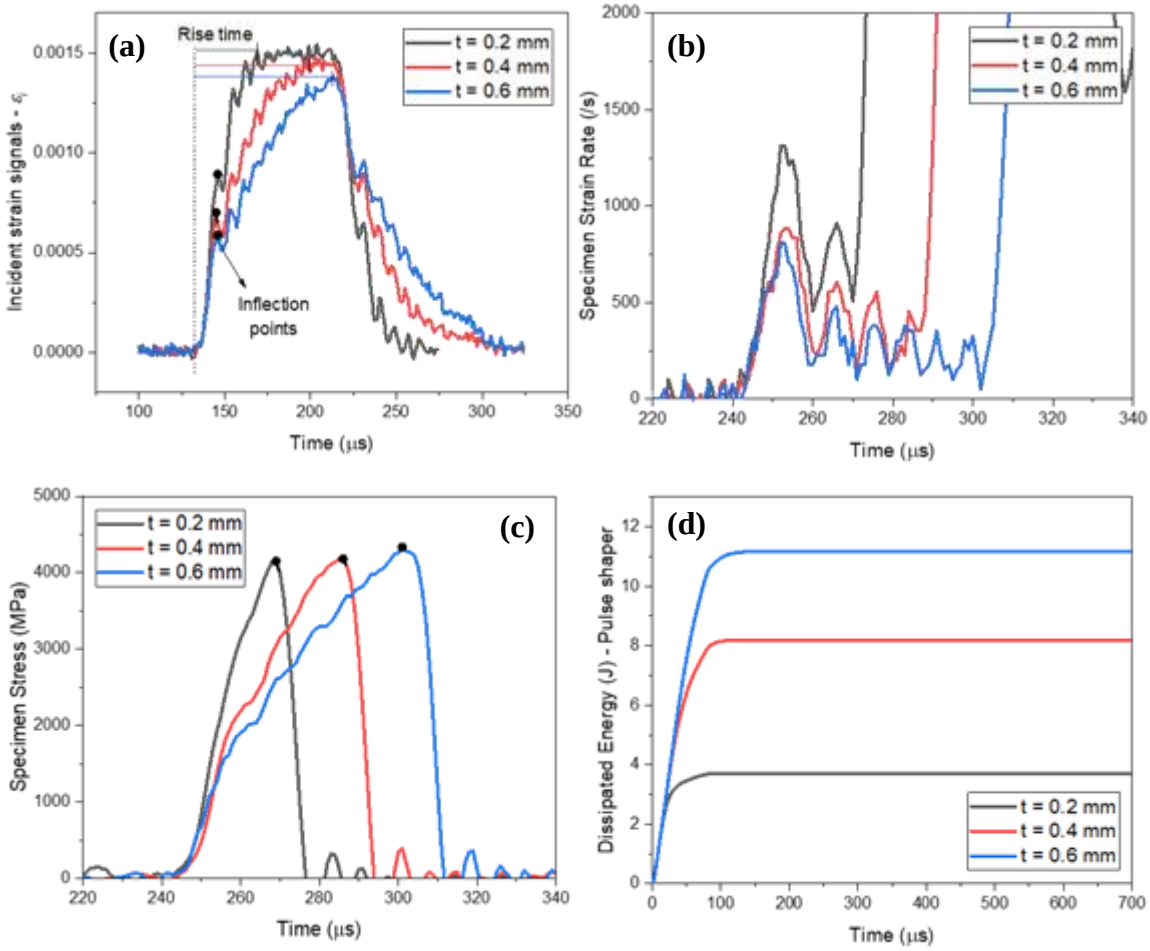

Figure 4.9: Effects of varying pulse shaper thicknesses on **(a)** Incident strain signals **(b)** Specimen strain-rate **(c)** Specimen stress **(d)** Plastic dissipated energy during pulse shaper deformation (Striker v = 15m/s; Pulse shaper d = 5mm, t = 0.2mm).

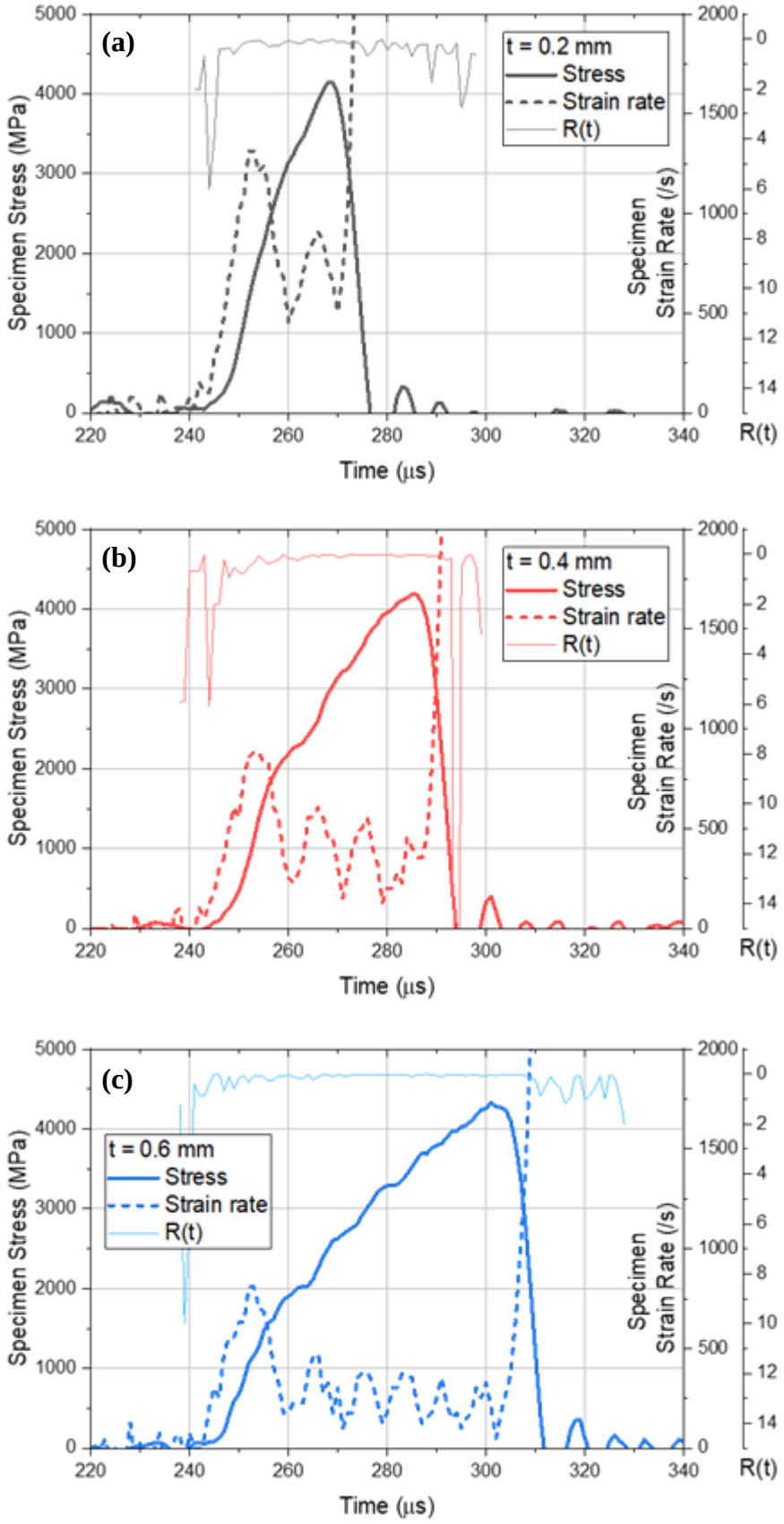

Figure 4.10: Stress, strain rate and $R(t)$ curves of specimen with respect to time corresponding to each of the pulse shaper thicknesses **(a)** 0.2mm **(b)** 0.4mm **(c)** 0.6mm.

4.1.3. Comparative study

FE simulations are carried out using a 200 mm striker impacting at 15m/s with a Φ6 mm x 0.6 mm copper pulse shaper, by varying the specimen materials in order to compare the response of silicon carbide, boron carbide and alumina. This pulse shaper was chosen as here dynamic equilibrium is achieved faster and is maintained for the longest time. All other part dimensions and properties remain unchanged. Effect of geometry change for each material has also been discussed.

- *Comparison between SiC, B_4C and Al_2O_3*

The strain rates achieved by each of the ceramic is marked in Fig.4.11a and they are approximately in the 300 /s – 400 /s range, the variation being narrow enough to allow comparison of the material response. The dynamic compressive strength of boron carbide is very low compared to silicon carbide (highest compressive strength) and alumina ceramics, as seen in Fig.4.11c. The former also deforms rapidly. The failure strain values for each is given in the stress-strain graph (Fig.4.11b).

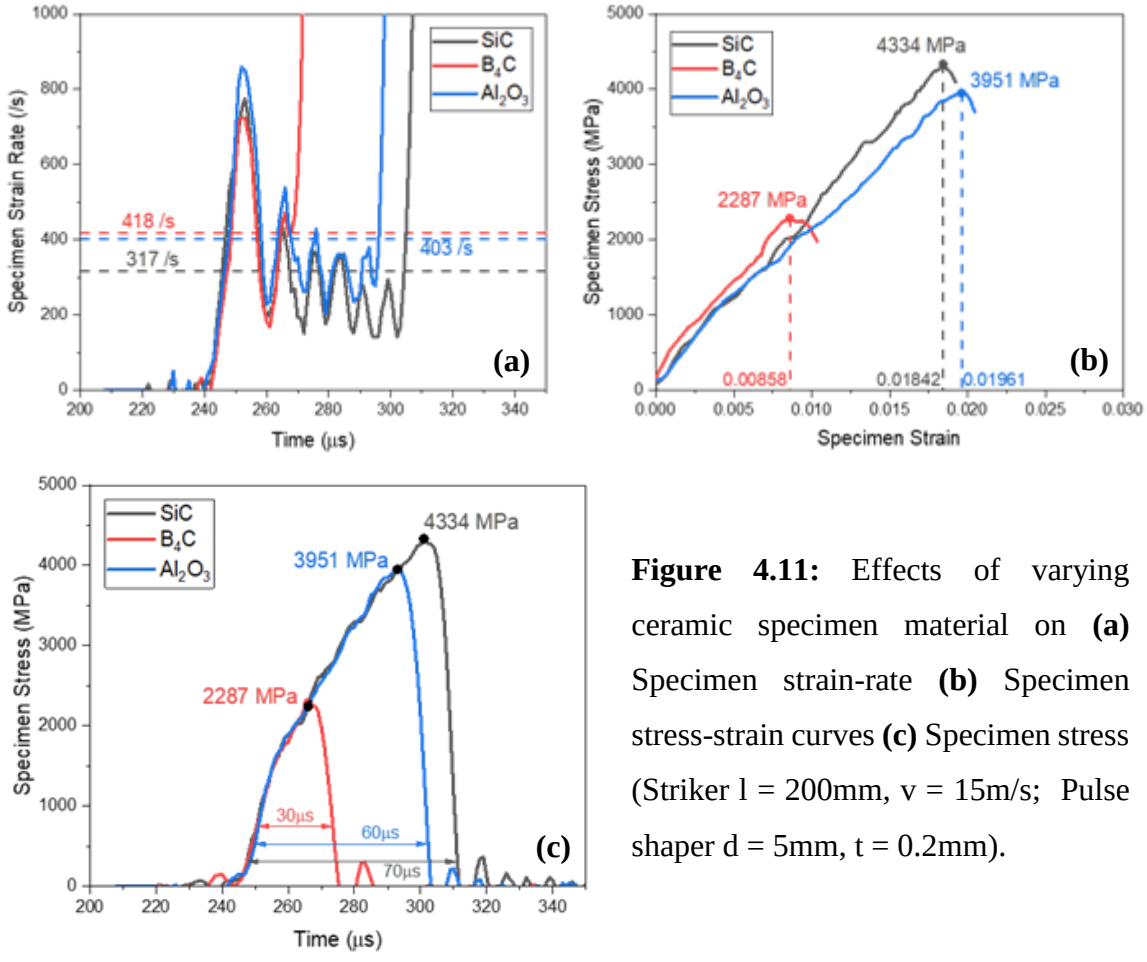

Figure 4.11: Effects of varying ceramic specimen material on **(a)** Specimen strain-rate **(b)** Specimen stress-strain curves **(c)** Specimen stress (Striker l = 200mm, v = 15m/s; Pulse shaper d = 5mm, t = 0.2mm).

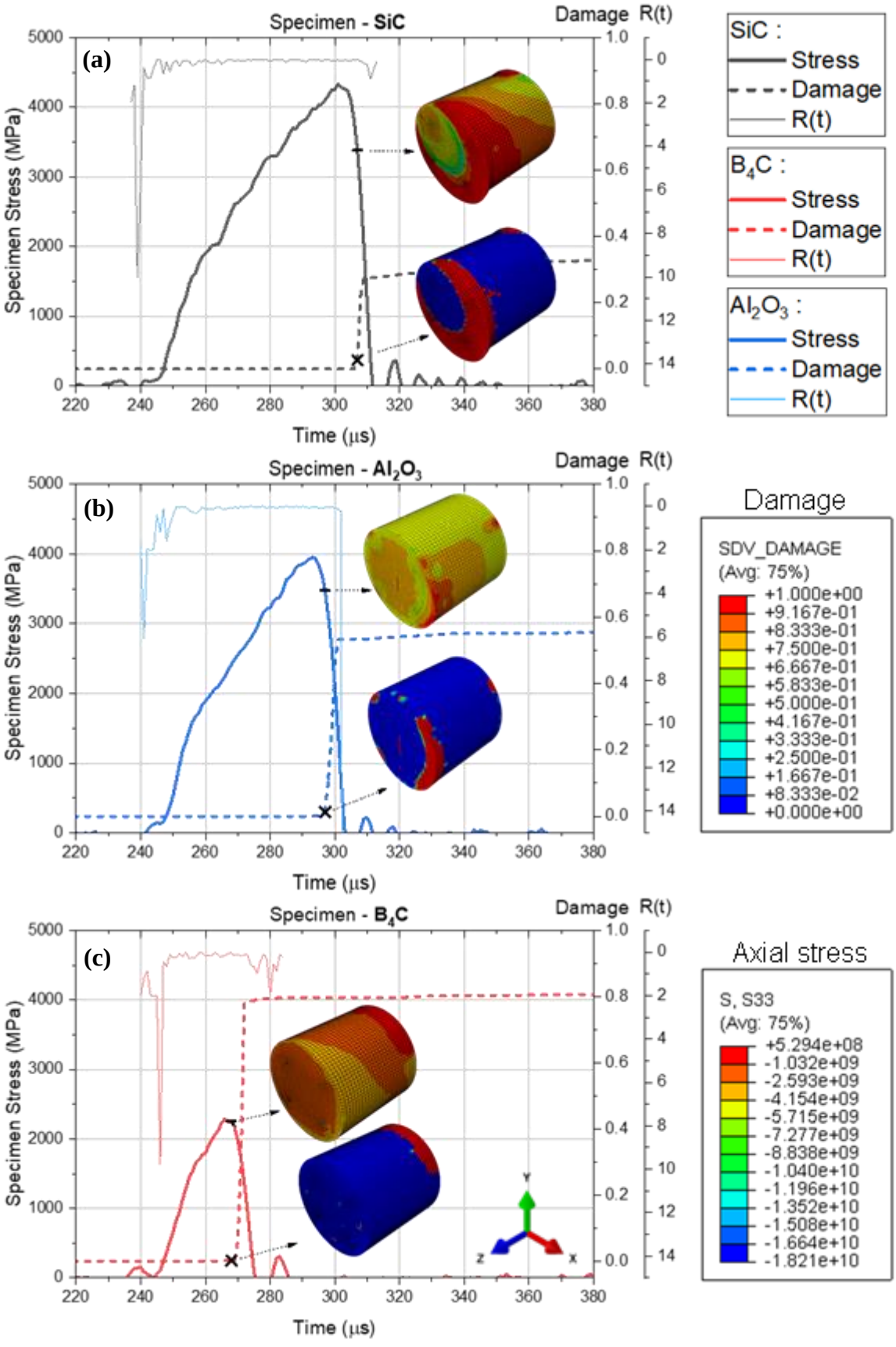

Figure 4.12: Specimen stress, strain rate and $R(t)$ curves for **(a)** SiC **(b)** B_4C **(c)** Al_2O_3.

Fig.4.12 from the preceding page includes individual plots for stress, $R(t)$ and damage each of the ceramics with respect to time. The $R(t)$ values show that equilibrium is achieved in all three ceramics and thus the experimental simulations are valid. Damage represents the JH-2 damage parameter (D) which is 0 when material is intact and gradually rises to 1 with increase in damage. It increases right after peak stress, implying that damage begins in the specimen only once peak stress is achieved. SiC being the ceramic with the highest magnitude of peak stress is also the least damaged, with maximum average D value to be 0.4. This is also reiterated in Fig.4.13 showing the damage in each of the specimen at a selected time. Even though the D value of Al_2O_3 is higher than B_4C, it looks like Al_2O_3 is more damaged when compared at 310 µs. But Al_2O_3 contains more undamaged (blue) elements resulting in lower D value. The damage and axial stress states of the specimen at the point where damage begins is illustrated in each of the Fig.4.12 plots. It can be observed that damage begins from the circumference of the specimen where stress concentration is generally high for brittle materials. The impact side of SiC and Al_2O_3 are first damaged, and B_4C on the other hand damages at the opposite end initially, results being consistent with previous studies [29, 31]. This implies that failure started in SiC and Al_2O_3 before the stress wave has passed through the entire thickness of the sample. The stress contours confirm the fact that in ceramic materials damage happens due to tensile stress rather than compressive (as it can be seen that the region where axial stress is tensile is same as the red region in damage contour), in line with studies on damage progression in armour ceramics due to impact (theory discussed in Section 1.3). So in B_4C, enough number of reverberations have occurred that the tensile wave reflection occurred at the transmission end, unlike the other two were the stress limit of material exceeded beforehand and this can be attributed to the wave speed $\left(c = \sqrt{\frac{E}{\rho}}\right)$ which is highest in B_4C.

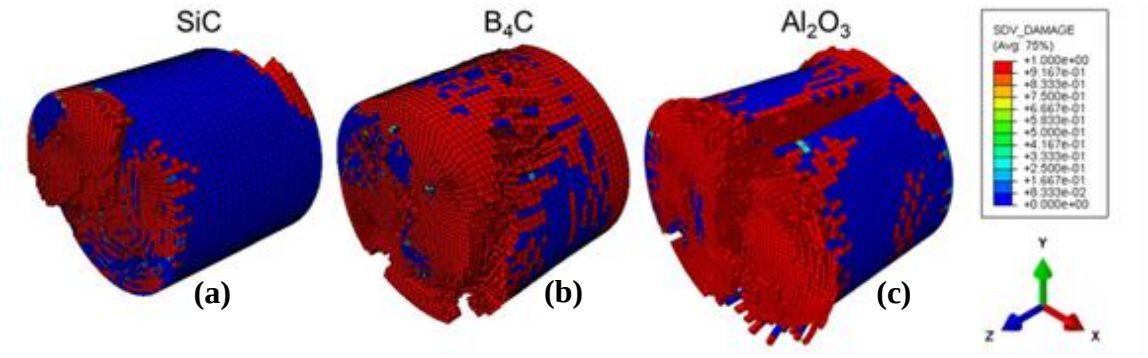

Figure 4.13: Damage contours at 310 µs of the simulation of **(a)** SiC **(b)** B_4C **(c)** Al_2O_3.

The amount of energy the material absorbs during deformation is another important property to be compared, useful to understand if it is apt for use in armor applications. As introduced earlier, ceramics are backed with a metallic plate when used as armor. The fracture of the ceramic creates more pathways to distribute the projectile's kinetic energy to a larger area of the backing plate, which then absorbs this energy. If the ceramic material consumes energy for deformation and fracture, lesser energy will be transferred to the metal plate. The same analogy can be applied to high strain rate deformation using SHPB.

The absorbed energy by the specimen is the remaining part of the incident energy after reflection and transmission of stress waves, given by –

$$E_a = E_I - E_R - E_T \tag{4.4}$$

where, E_I, E_R and E_T are calculated using Eqn.1.2.

For the considered SHPB simulations, since volume of specimen is small, the energy used for its deformation will also be low compared to the incident and reflected energies, as shown in Fig.4.14 for SiC. Fig.4.15 compares the energy absorbed by all three ceramics and conveys that SiC described by the selected JH-2 parameters is a better candidate for armour applications due to higher absorption of energy during deformation. Moreover, its high compressive strength, lower damage and longer deformation time, reaffirms the finding.

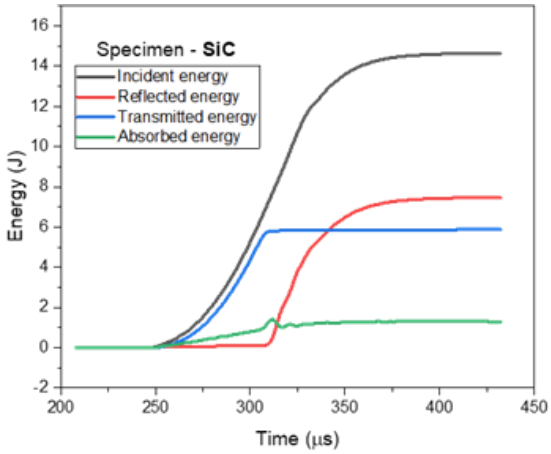

Figure 4.14: E_I, E_R, E_T and E_a for SiC during simulated SHPB test. B_4C and Al_2O_3 also showed similar trends.

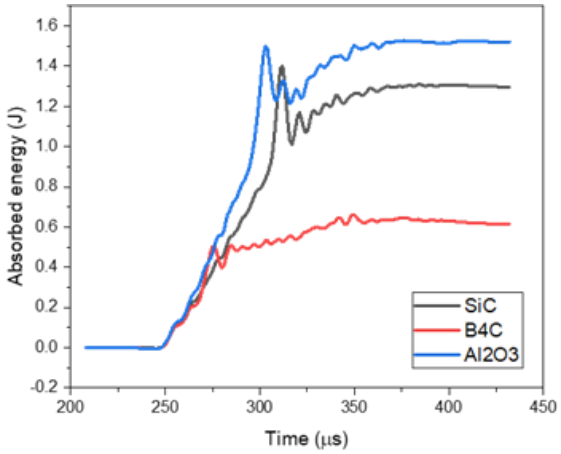

Figure 4.15: Energy absorbed (E_a) by each of the specimens during simulated SHPB.

- *Comparison between different specimen geometries :*

In order to understand the effect of specimen geometry on material response, numerical SHPB tests with cubical specimens of similar aspect ratio are compared with the previously discussed results where cylindrical samples were used. The material-wise trends displayed are similar to cylindrical specimens, hence not repeated. The strain rates achieved by the cubical specimens are very slightly higher than cylindrical specimens, as shown in Fig. 4.15. Only B4C shows a variation of beyond 100/s.

In all three cases of stress/damage vs. time curves (separately shown for each ceramic in Fig.4.17), the cubical specimens display a reduction in compressive strength, and in turn an increase in damage. As discussed in previous section, stress concentration is observed at the circumference of cylindrical specimens while in cubical specimens it is at the corners. A comparison between the axial stress contours at a selected time of each of the specimens is illustrated in Fig.4.16 and it is visible that the cubical corners are stressed more than the cylinder circumference, the difference being prominent in the case of B4C. This along with the slightly higher strain rates achieved by cubical specimens attribute to decrease in compressive strength and early material failure. Correspondingly greater strength reduction is seen in B4C.

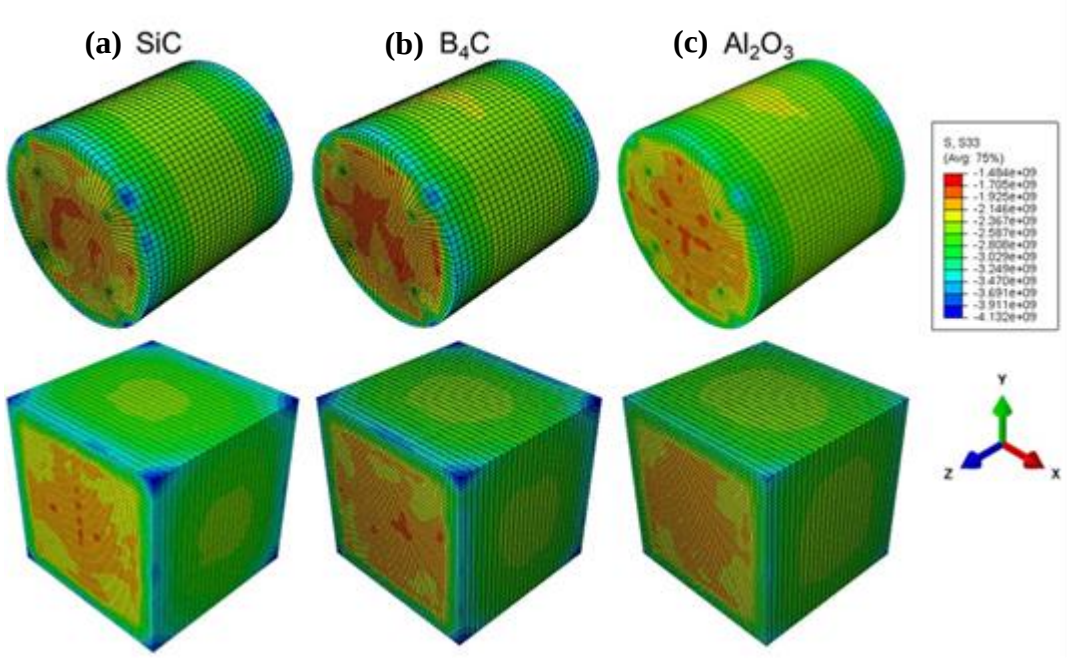

Figure 4.16: Axial stress contours at 265 µs of cylindrical and cubical specimens of **(a)** SiC **(b)** B_4C **(c)** Al_2O_3.

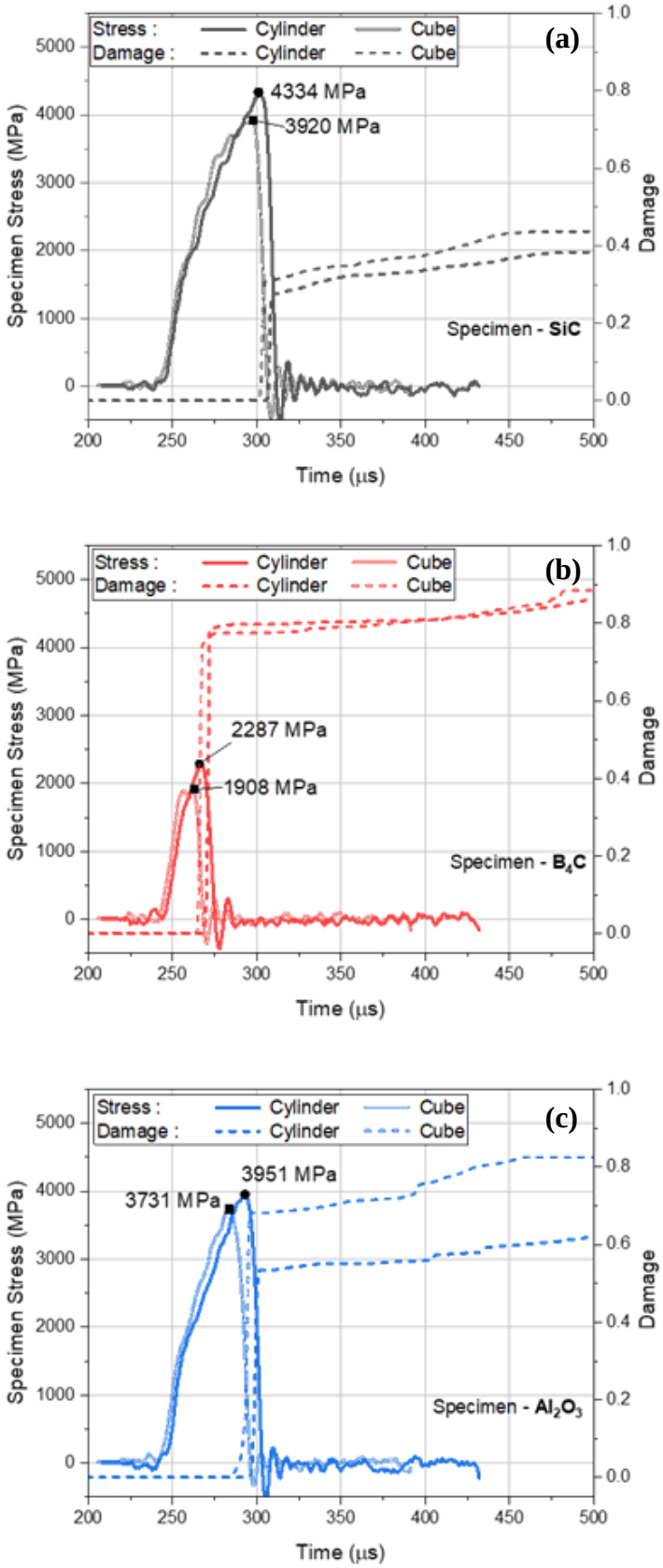

Figure 4.17: Comparison of axial stress and damage curves between cylindrical and cubical specimens of **(a)** SiC **(b)** B_4C **(c)** Al_2O_3.

4.2. Experimental results

4.2.1. Initial microstructures

The optical micrographs of the unetched, polished samples of rb-SiC, as given in Fig.4.18, reveal large regions of SiC appearing as grey with residual-Si occupying the pores appearing white in colour. The dark spots are due to material pull out which occurred during the grinding and polishing of the specimen surface. A comparison between the microstructures of the inner and hexagonal face of the sample as represented in Fig.4.19 shows that the Si content is comparatively higher in the hexagonal face, which is the cross-section along the sintering direction. This might be due to the Si infiltration process and it makes the investigation of material anisotropy across both the directions necessary.

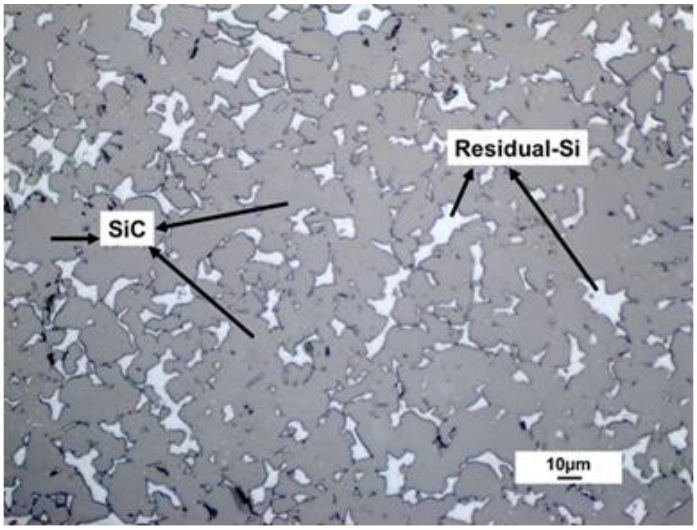

Figure 4.18: Optical micrographs of unetched, polished hexagonal surface of rb-SiC.

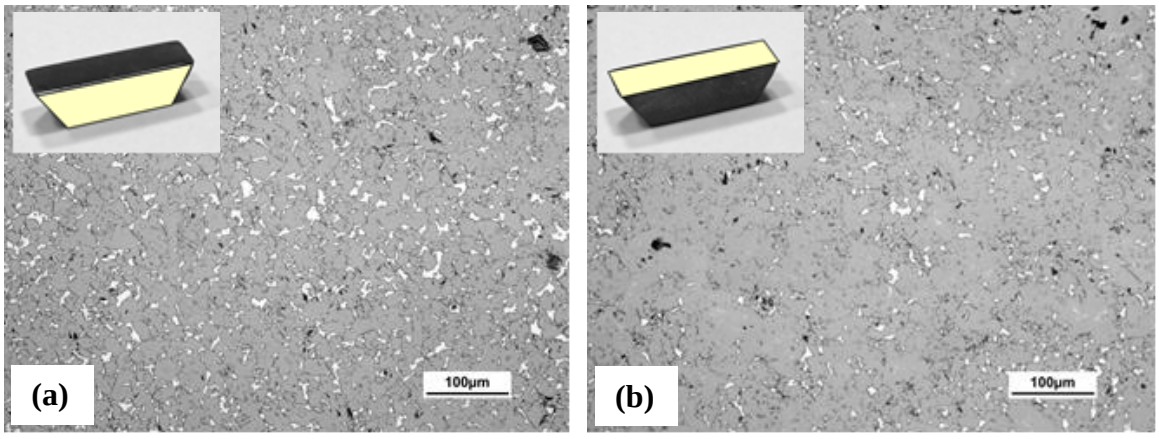

Figure 4.19: Optical micrographs of rb-SiC showing variation in residual-Si content in **(a)** hexagonal face **(b)** inner face, as depicted in the inlet figure.

The SEM examination of the specimen surface shows that the residual-Si and SiC can be differentiated topographically due to polishing relief and atomic number contrast between them. Unlike the optical micrographs, the SiC grains revealed in these SEM images exhibit regions of different shades (Fig.4.20). The darker (sometimes lighter) core is the original SiC used in the fabrication process and the outer lighter shade coating corresponds to the new SiC formed through the reaction bonding process, which has been epitaxially deposited over the initial SiC particles. The boundary between them is sharp. This unusual secondary electron SEM contrast has been explained elsewhere by Sawyer and Page [50], and it is basically due to different impurity levels between the two phases.

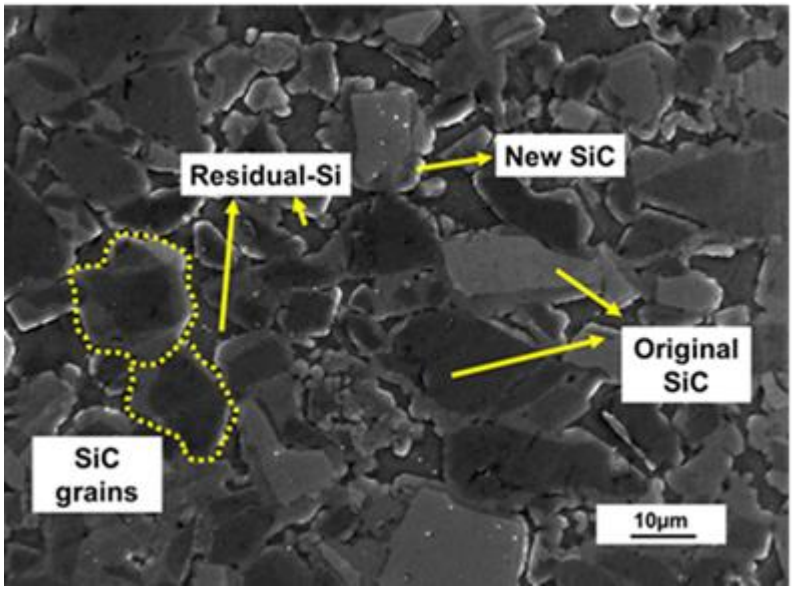

Figure 4.20: Representative secondary electron SEM image of rb-SiC.

4.2.2. Mechanical characterisation using hardness

- *Variation in hardness with respect to load*

Hardness is the resistance offered due to localized plastic deformation caused by mechanical indentation. The size of the indents generated are measured and the following equations are used to calculate the Vickers and Knoop hardness number –

$$H_V = \frac{1854\ F}{D^2} \qquad (4.5a)$$

$$H_K = \frac{14229\ F}{d^2} \qquad (4.5b)$$

where, H_V = Vickers hardness (kg/mm^2) / VHN

H_K = Knoop hardness (kg/mm^2) / KHN

F = Indentation load (g)

D = Average of diagonals of Vicker indent (µm)

d = Longest diagonal of Knoop indent (µm)

The low magnification SEM micrographs of Vickers indents at 1N loads show that the material cracked considerably at the indent edges (Fig.4.21a). This was much more extensive and indents became almost indiscernible at 2N load as Fig.4.21b shows. Calculations were carried out using few of the coherent indents were the diagonals could be properly measured. In the case of Knoop indents, cracks formed from 0.5N load itself, as shown in the representative SEM images in Fig.4.22. But still the length of the indent is very sharply visible and therefore no difficulty was faced during calculations.

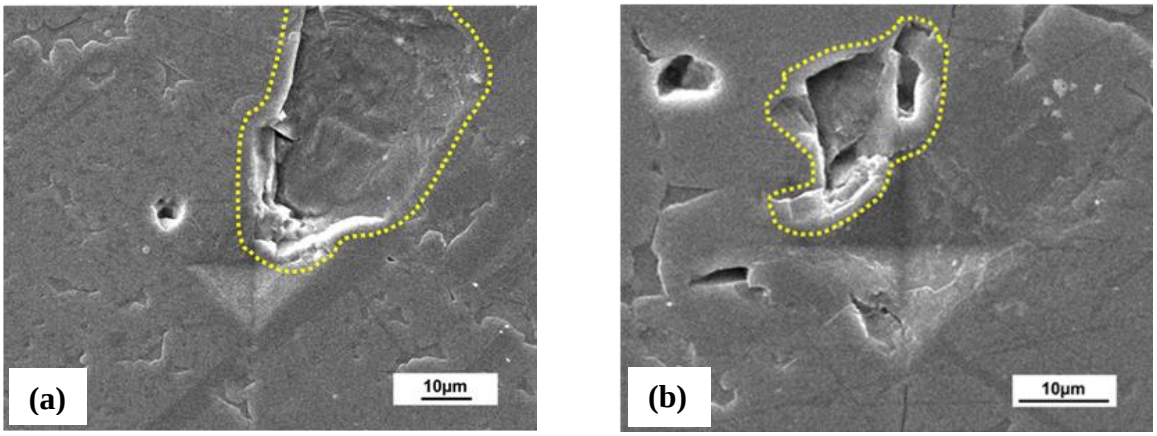

Figure 4.21: Representative SEM images of Vickers indents on rb-SiC displaying cracks at the indent edges when loaded at **(a)** 1N **(b)** 2N.

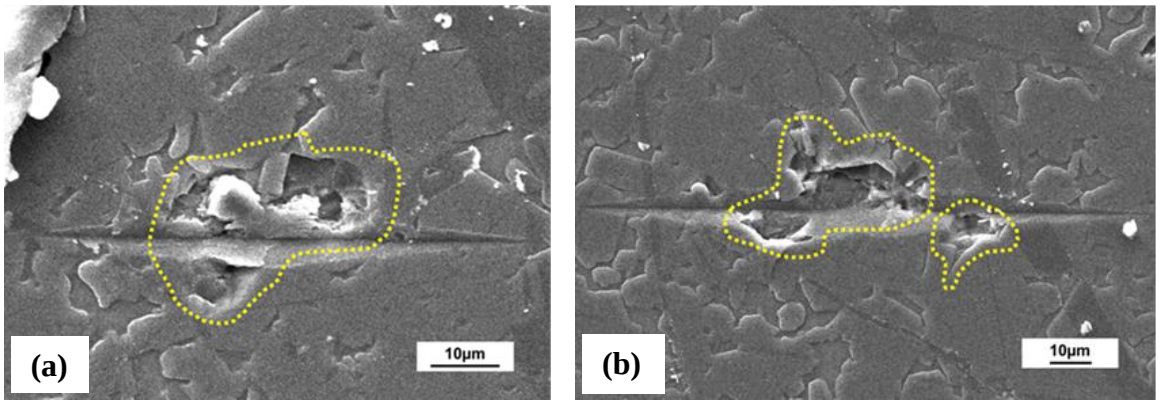

Figure 4.22: Representative SEM images of Knoop indents on rb-SiC displaying cracks at the indent edges when loaded at **(a)** 0.5N **(b)** 1N.

The variation in indent size and thereby hardness number with applied load was studied for Vickers as well as Knoop indentation impressions, taking 5 and 3 indents for each load for both techniques respectively. A decrease in Vickers (Fig.4.23a) and Knoop (Fig.4.23b) hardness is observed in rb-SiC with increasing load, which stabilizes beyond 1N. This trend is generally referred to as indentation size effect (ISE) and is commonly observed in silicon carbide [51, 52], including reaction-bonded SiC [53]. The KHN values were lower compared to VHN.

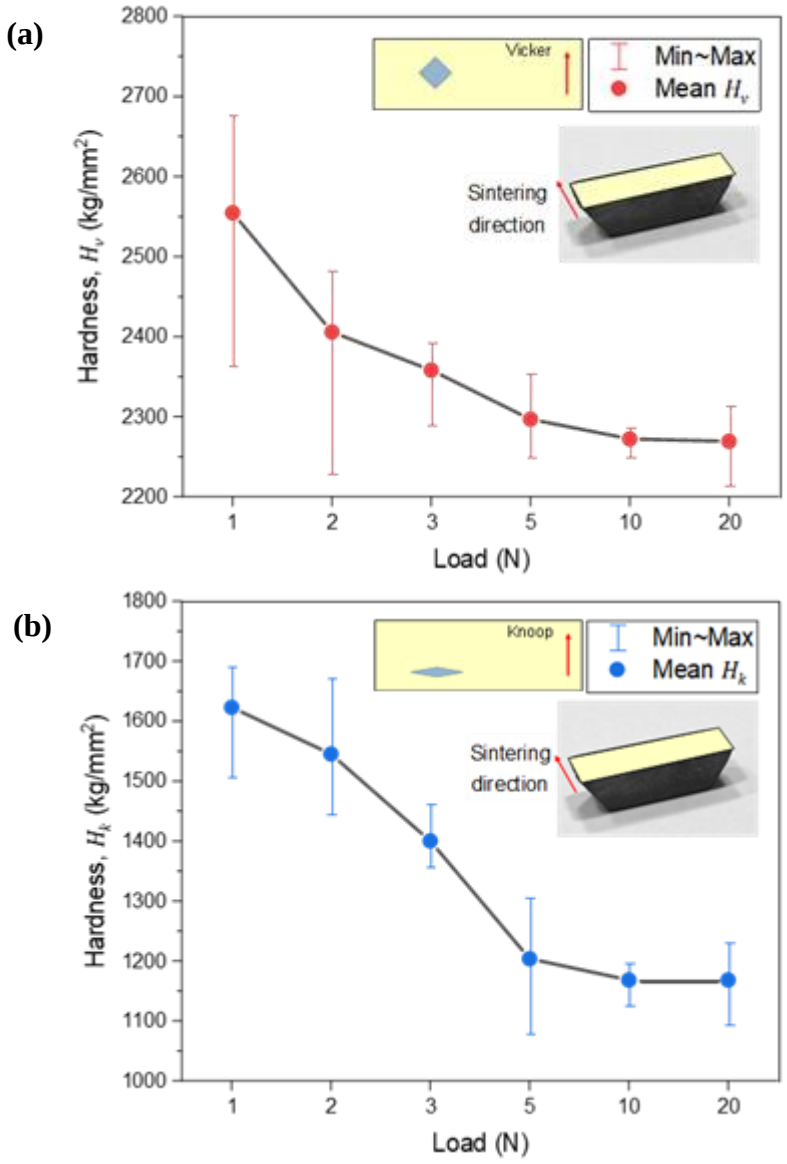

Figure 4.23: Variation of hardness number with maximum applied load for loads ranging from 1N to 20N for **(a)** Vickers indentation **(b)** Knoop indentation.

- *Calculation of specimen's Vickers hardness*

Since VHN becomes almost constant at and beyond 10N, 10 indents were made on the inner face at this load and its average was used to calculate the material's hardness. Table 4.1 shows the obtained impression sizes and calculated VHN values.

Table 4.1: Observed Vickers indent sizes and calculated Vickers Hardness Number.

Vickers indent dimensions		**VHN (kg/mm^2)**
D_1 (µm)	**D_2 (µm)**	
28.03	28.92	2286.5
29.6	28.7	2181.8
27.35	29.6	2286.56
28.48	28.92	2250.8
30.27	26.68	2286.56
29.15	29.37	2165.51
30.04	26.68	2305.14
29.15	29.82	2132.5
29.37	29.15	2165.5
27.35	30.04	2251.6

Average VHN was approximately 2231.247 kgf/mm^2, which is a hardness of 21.866 GPa at 1 N or 1000g load, calculated as follows –

$$\text{Average VHN} = 2231.247 \ {}^{kgf}/_{mm^2}$$

$$= \ 2231.24 \times 9.81 \ {}^{N}/_{mm^2}$$

$$= 21866.2206 \ MPa$$

$$= \mathbf{21.866 \ GPa} \sim 22GPa \text{ (1000g load)}$$

- *Investigation of hardness anisotropy using Knoop indentation*

The average of Knoop hardness loaded with indent diagonal parallel and perpendicular to sintering direction is given in Fig.4.24. 6 indents each were taken. It is evident that there is no hardness anisotropy exhibited by the specimen, unlike what single crystals of SiC and other ceramics have displayed.

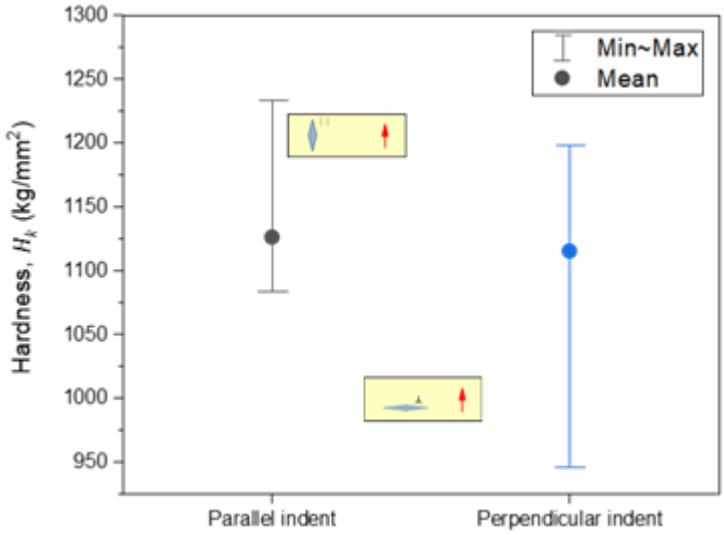

Figure 4.24: Knoop hardness numbers for indent diagonals parallel and perpendicular to sintering direction, to investigate hardness anisotropy of rb-SiC.

4.2.3. Dynamic compression studies

- *Results of uniaxial compression tests using miniaturised-SHPB*

The strain signals obtained during the high strain-rate deformation of the specimens for a trials at 2 bar and 4 bar pressure are plotted in Fig.4.25a and b respectively. In both cases, incident signals of both trials coincide precisely, implying that the input force and pulse shaping is repeating and thereby can be used to for further investigation. As introduced previously, the reflected signals gives the trend shown by the strain-rate achieved in the specimen and the transmitted signals represent the stress-time curve. It is observed that the magnitude of transmitted signal is higher at 4 bar pressure and duration of the signals are also higher.

It is to be noted that among all the SHPB trials, a few showed incorrect signals where the reflected signals showed double peaks without any constant strain rate region during the deformation process (given in Fig.4.25c). These trials are not considered for the final calculation of specimen stress-strain characterisation.

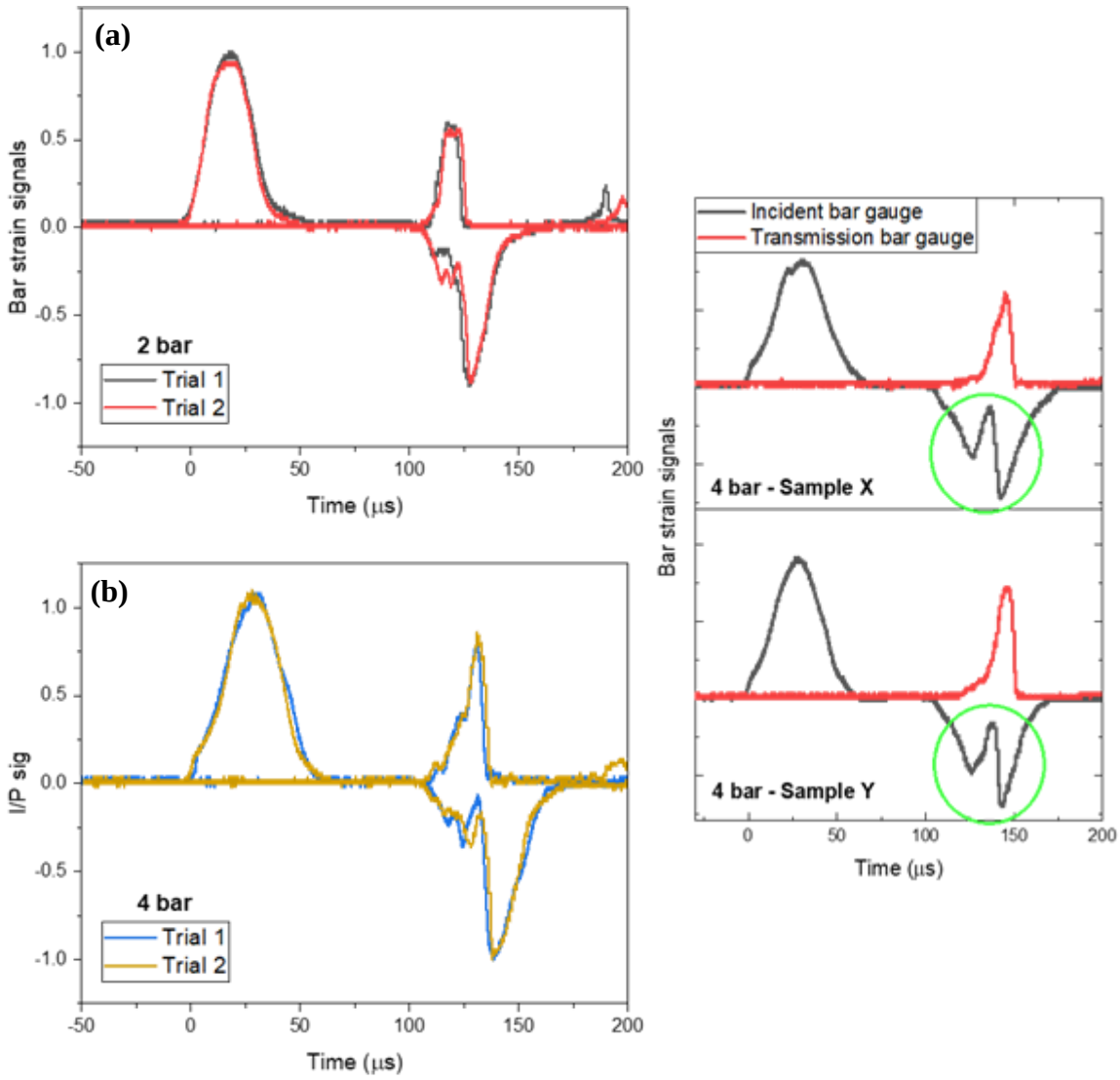

Figure 4.25: Bar strain signals obtained from strain gauges at the midpoint of both input and output bars for m-SHPB trials carried out at pressure **(a)** 2 bar **(b)** 4 bar ; **(c)** Examples of invalid trials where constant strain-rate deformation did not occur in the specimen, and double peaks (marked in green) were observed in the reflected signals.

- *rb-SiC specimen stress-strain characterisation*

Fig.4.26 gives the stress and strain rate vs. time for each of the trials individually at both pressures. It can be observed that constant strain rate is achieved for both trials under 2 bar pressure, while under 4 bar pressure, specimen deformed at constant strain rate only in one of the trials. The strain rates vary from 2000/s to about 3500/s when the pressure is 2 bar whereas for 4 bar pressure it is approximately 3000/s. The peak stress values are also marked.

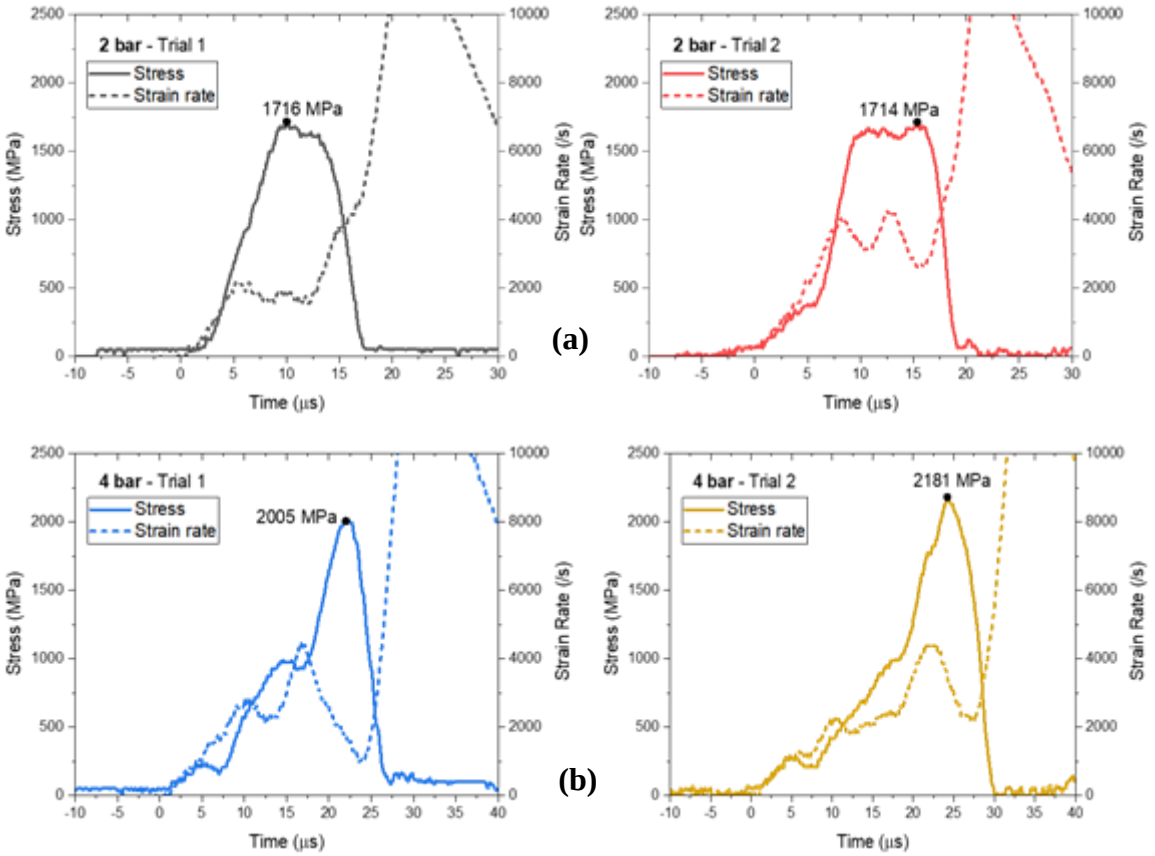

Figure 4.26: Specimen stress and strain rate vs time at **(a)** 2 bar **(b)** 4 bar pressure.

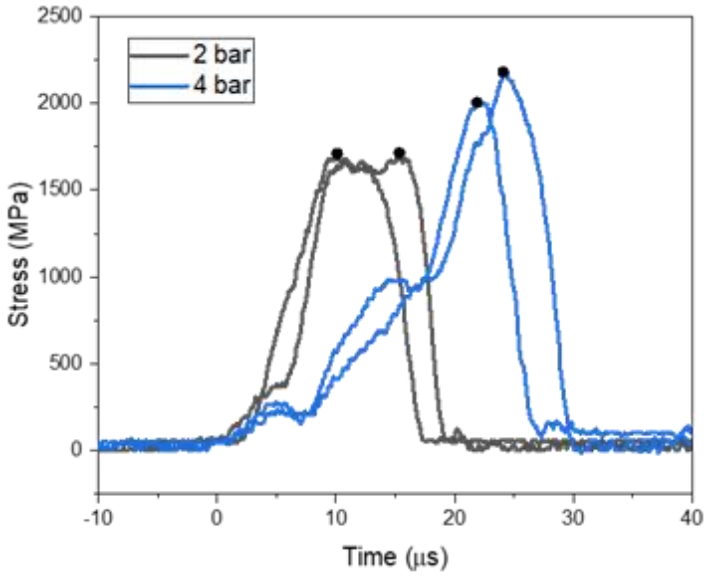

Figure 4.27: rb-SiC specimen's stress-time curves for all experimental trials.

All stress-time curves are together comprised in Fig.4.27 and it clearly shows the rise in compressive strength of the rb-SiC specimen at higher pressure, with an increase in deformation time too. Failure strain also increases, as the dynamic stress-strain curves of

Fig.4.28 indicates. They are of the range 2-5% which is very high for brittle ceramic material, for which the strain to failure is ideally less than 1%.

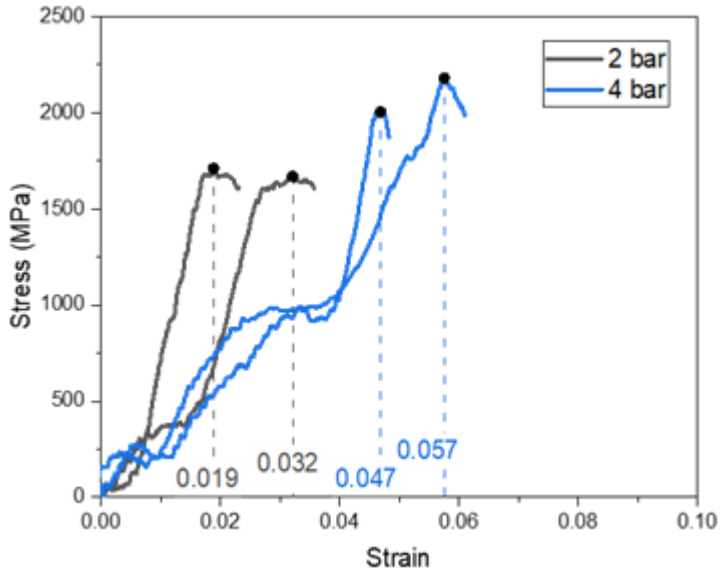

Figure 4.28: rb-SiC specimen's stress-strain curves for all experimental trials.

- *Preliminary fracture analysis*

The fragments obtained after the experiment are extremely small in size and powdered in nature. Most of them stick to the base or the ends of the platens, and remaining were collected. Size distribution is not studied because some very small fragments are not considered. Preliminary analysis of the fracture surface of the collected fragments is carried out using SEM and the images at different magnifications were taken.

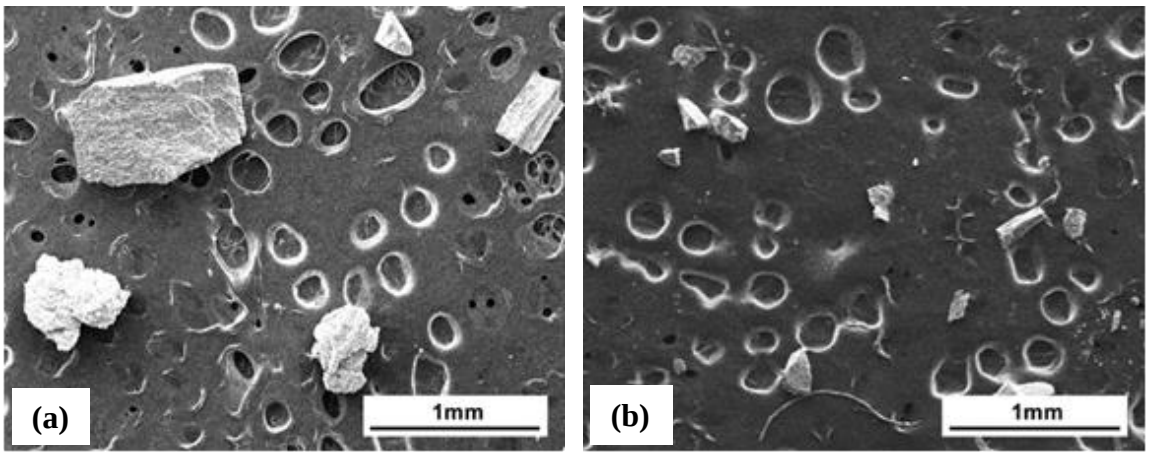

Figure 4.29: Low magnification SEM images of fragments collected on carbon tape, deformed at a pressure of **(a)** 2bar **(b)** 4 bar.

The collected fragments resulting from deformation at both pressures exhibits non-uniform size distribution ranging from 30 to 800 μm. Fig.4.29 illustrates that the fragments are comparatively smaller for the 4 bar pressure case which is obvious because previous studies have shown reduction in fragment sizes as the strain rate of deformation increases. Quantitative comparison is not conducted because only a part of the fragments could be collected. The comparatively larger samples are likely to have formed at the circumferential edges of the sample as was observed during the FE simulations, and the smaller ones from inside. These fragments are generally flaky shaped and are mostly covered with much smaller debris pieces (shown in Fig.4.30).

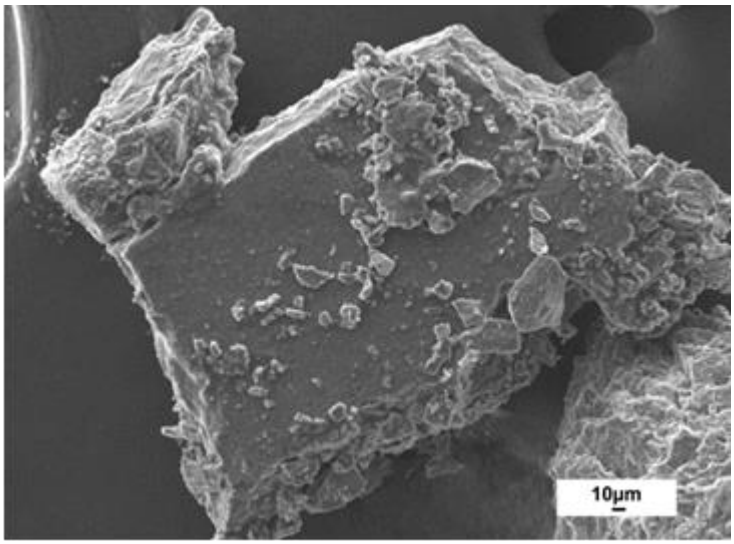

Figure 4.30: SEM image of flaky shaped rb-SiC fragment with small debris particles.

A closer look at the fragments in Fig.4.31 reveal the presence of uneven (region B) as well as smooth and even surfaces of fracture (region A). This is an indication of a combined intergranular and transgranular mode of fracture. Intergranular fracture involves crack propagation along the grain boundaries giving rise to uneven surfaces with sharp edges as shown in Fig.4.32a, while transgranular crack propagation is within the grains, cutting through them, leading to formation of smooth surfaces as depicted in Fig.4.32b.

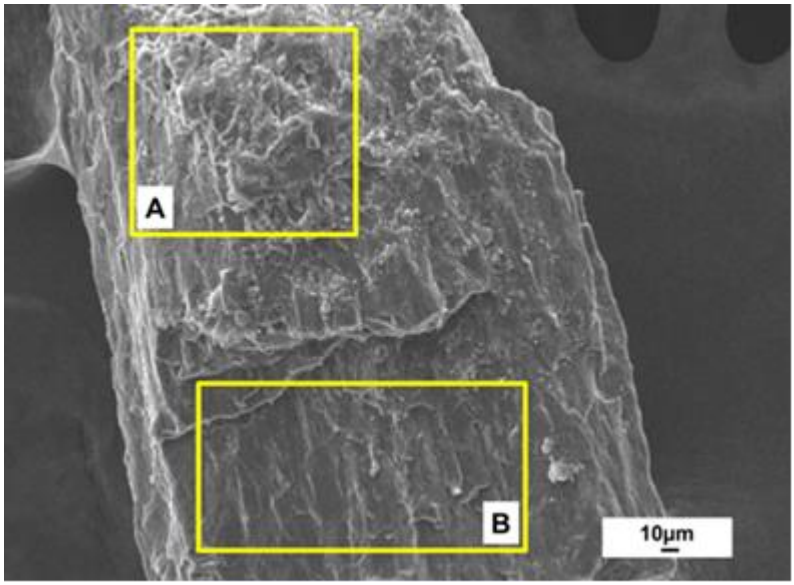

Figure 4.31: Representative SEM image of dynamically deformed rb-SiC fragment featuring fracture surface, displaying mixed mode fracture. Region A depicts intergranular fracture, while region B is of transgranular fracture.

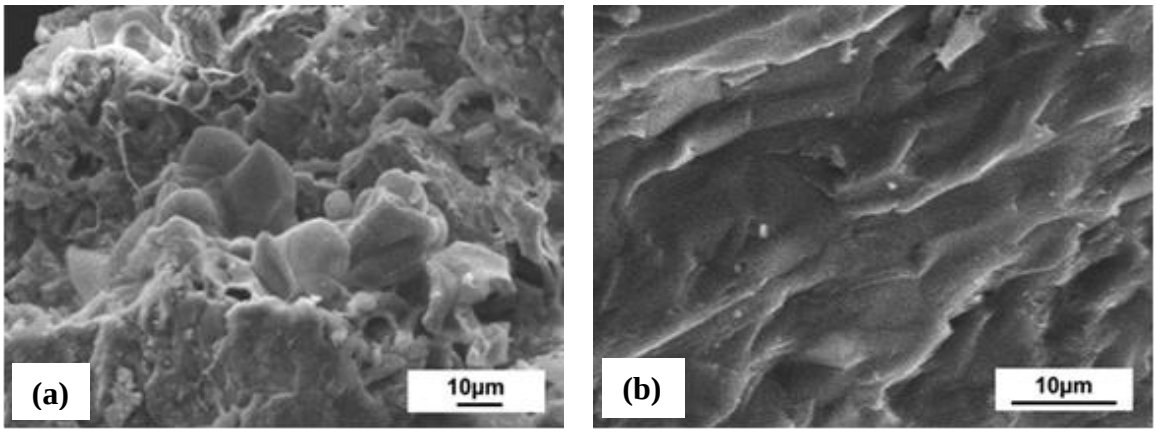

Figure 4.32: Representative SEM micrographs depicting high strain rate fracture mechanisms in rb-SiC where **(a)** is predominantly intergranular, while **(b)** is predominantly transgranular.

4.3. Discussion

4.3.1. Variation of hardness with load

The decrease in hardness with increase in maximum applied load cannot be termed as ISE, as commonly found in literature, because here the specimen cracks before the size stabilizes and the observed decrease in Vickers as well as Knoop hardness is due to this crack and its propagation, rather than any size effect. ISE is a phenomenon usually observed at nanoscale, and it is a common misnomer to define reduction in hardness due to crack formation also as indentation size effect.

4.3.2. Effect of inefficient specimen preparation on SHPB results

Even though the SHPB trials gave valid results during the high strain rate uniaxial compression of the machines rb-SiC specimens, it is matter of concern why double peaks of reflected signals were observed in a few of experimental trials, with no constant strain rate being achieved. In order to understand if the machining of samples has any effect to this, the previously taken images of the sample using stereo microscope is analyzed.

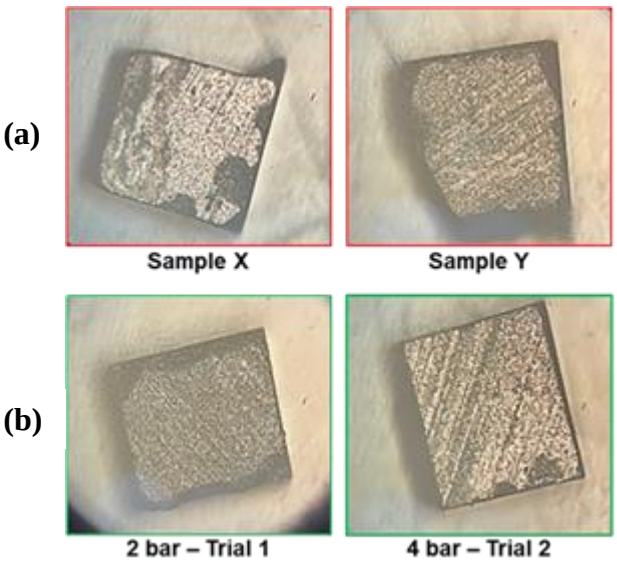

Figure 4.33: Images showing specimen cross-section of the specimens used in the SHPB experiments, in which **(a)** gave rise to double peaks in reflected signals, while **(b)** gave valid results with constant strain-rate deformation.

The first set of images (Fig.4.33a) correspond to sample X and Y which gave the double peaks in Fig.4.25c, and it is very clearly visible that these have unpolished burrs at the edges and the cross section which is not perfectly square. On the other hand, the specimens used

for the valid experiments, given in Fig.4.33b do not show any burrs or protrusions and has a planar cross-section. These imperfections is machining lead to deviations from uniaxiality in stress propagation, therefore giving signals which cannot be used to characterize the material.

Low-speed diamond cutting will always lead to such machining burrs, whose effect will exaggerate during SHPB experiments because the sample size is very small. It is impossible to polish specimens of this size for surface finish because of the high hardness of SiC. More accurate cutting techniques suitable for hard and brittle ceramics will help in precise sample preparation and thereby give repetition of results.

4.3.3. Specimen stress-strain characteristics

The dynamic compressive strength of of the rb-SiC specimens is observed to be 1715 MPa at 2 bar pressure and 2093MPa at 4 bar pressure on an average. This increase in peak stress values displays the strong strain-rate sensitivity of the material which is attributed to inertia-dominated crack growth from flaws, rather than material property. SiC processed through different routes like sintering and hot-pressing and other advanced ceramics also exhibit similar sensitivity above a strain rate of 10^3/s. Analysis of crack initiation and propagation during high strain-rate compression will help correlate the phenomenon with the reaction-bonded material's microstructure, but due to lack of high-speed imaging techniques, the same has not been done.

The failure strain observed are high compared to the usual 1% strain to failure of brittle ceramics. The reason for the same might be the very small size of the specimen, and experimentation at miniaturised scale rather than conventional SHPB. The specimen size itself is very small, but the crack initiated from flaws due to the material reaching its compressive limit remains similar. This amplifies the strain to failure, and this effect of slightly increasing failure strains in smaller specimens has been verified using simulations. Similar decrease in failure strain has been observed by Zhao et. al. [54] during tensile testing of miniaturised specimens.

4.3.4. Fracture mechanism

The preliminary fracture studies and surfaces in Fig.4.31 illustrates that rb-SiC undergoes a mixed-mode type of fracture, involving both intergranular and transgranular crack propagation. Initially, during lower strain rates below the critical level, micro-cracks initiate

and propagate along the grain boundaries, similar to crack growth and propagation during quasi-static loading [29]. This is due to the comparatively weak interfacial strength. But as and when the loading rates increase the critical value, the strain energy released by the tip of these propagating cracks is sufficiently high to cut through the grains and lead to transgranular fracture. Thus in rb-SiC, dynamic compression is governed by both intergranular and transgranular modes of fracture, schematically illustrated in Fig.4.34.

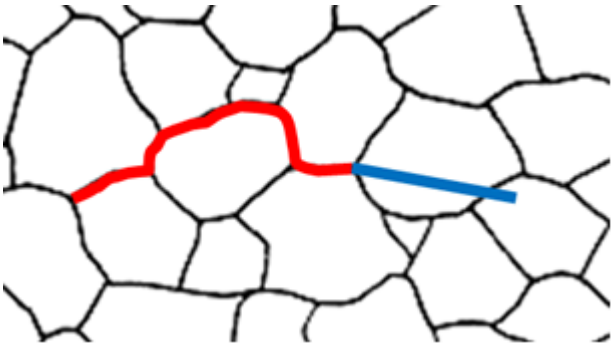

Figure 4.34: Schematic describing the fracture mechanism observed in rb-SiC specimens. Red line represents intergranular fracture along the grain boundaries, followed by transgranular fracture as depicted by the blue line.

Chapter 5 :

Conclusions and Future Scope

In this work we computationally and experimentally studied the high strain rate deformation behavior of advanced ceramics used in armour applications, with a special focus towards the study of influence of SHPB parameters specimen characteristic curves.

The major conclusions made from the computational results are as follows –

i. All the parameters studied, namely striker bar velocity and length, and pulse shaper dimensions, have a direct influence on the incident strain signals, thereby shaping the pulse. Rise time can be controlled by a proper combination of impact velocity and pulse shaper thickness. This concept was incorporated while carrying out the experiments also.

ii. Very low impact velocity or striker length gives rise to strain signals which are not able to generate enough force for deforming the sample. Only elastic unloading of sample is observed in such cases. At the same time, high velocity impact is also not recommended since constant strain rate is achieved for a very short time.

iii. There is not much change in results when diameter of pulse shaper varies, except that equilibrium is maintained for a little longer for larger diameters. Pulse shaper thickness affects rise time and thence the deformation period considerably.

iv. In all cases, results were correlated with the pulse shaper's plastic dissipation energy, in an attempt to explain results from a mechanistic point of view, usually not seen in other work.

v. Material-wise comparison helped in understanding how each of the ceramic behaves under high strain rate and also helped in analyzing internal damage and failure of the material (purely based on JH-2 parameters and not considering microstructural or mechanism based parameters). It has been observed that silicon carbide showed better property compared to alumina and boron carbide in terms of compressive strength, overall damage, elemental damage, and also when considering energy absorbed during the test. Even though alumina displayed higher values of compressive strength and lower average damage compared to boron carbide, the Al2O3 specimen axially splitted and underwent more local damage.

The above results cannot be considered as a generalized conclusion because it is solely based on the JH-2 parameters and there are cases when the strain-rate sensitivity of the specimen material is not captured by the model. But the trends shown can be used as a guideline for conducting SHPB experiments using SiC as the ceramic specimen for a particular geometry and dimensions. Similar simulations can be extended to other ceramic materials as well, and also by modelling varied apparatus components if required. A large number of trial experiments can be avoided by incorporating computer modelling in the early stages of experimentations. The comparative study provides a framework on analysis of computational results when material constitutive parameters can be determined for the specimen experimentally.

The high strain rate experimental study on reaction bonded silicon carbide led to the following conclusions –

i. Variation in both Vickers as well as Knoop hardness values was displayed by rb-SiC. No anisotropy in hardness was observed.
ii. The miniaturised SHPB results gave compressive strength values ~2000MPa in spite of the reported static compressive strength value to be 2500MPa. Ceramics generally show rise in strength values at higher strain rates. The reasons which might have led to this anomaly, along with why the stress signals obtained in some of the trials were invalid were also discussed.
iii. Preliminary analysis of the fracture surfaces of the fragments obtained showed that the rb-SiC underwent mixed (intergranular + transgranular) mode of fracture during dynamic loading.

The scopes for future work are as follows –

i. SHPB experiments can be performed such that the loading direction is perpendicular to the sintering direction. This can be compared with the present results to identify any case of anisotropy.
ii. Machining of the ceramic samples using industrially relevant methods like water jet machining or abrasive water jet machining will give test specimens with good surface finish and high parallelism. Since miniaturised-SHPB requires high levels of alignment, accurately machined samples might give better compressive strength.
iii. SHPB experiments can further be carried out using larger diameter bars (6 mm or 12 mm) which will help study deformation at a different strain rate. This will also

require slightly larger specimens, and thereby creating larger fragments for better understanding of fracture mechanisms.

iv. Dynamic properties of rb-SiC can be compared with that of sintered and hot-pressed SiC as well as other armor ceramic materials. Determination of material constitutive parameters using further experiments will be a breakthrough in carrying out simulations and more intensive studies.

v. The effect of other specimen-related parameters like effect of specimen-platen interface friction and specimen size effect can also be computationally studied.

REFERENCES

[1] S. Diego Lopes Da, N. Tian, and A. Marksteiner, “Trends in world military expenditure,2020.” Stockholm International Peace Research Institute, 2021.

[2] “Union Budget 2022-23,” Ministry of Finance, India, 2022.

[3] Paul J. Hazell, *Armour: Materials, Theory and Design*. CRC Press, Taylor & Francis group, 2016.

[4] I. G. Crouch, *The Science of Armour Materials*. Woodhead Publishing in Materials, 2017.

[5] I. G. Crouch, M. Kesharaju, and R. Nagarajah, “Characterisation, significance and detection of manufacturing defects in Reaction Sintered Silicon Carbide armour materials,” *Ceram. Int.*, vol. 41, no. 9, Part B, pp. 11581–11591, Nov. 2015, doi: 10.1016/j.ceramint.2015.06.083.

[6] W. W. Chen, A. M. Rajendran, B. Song, and X. Nie, “Dynamic Fracture of Ceramics in Armor Applications,” *J. Am. Ceram. Soc.*, vol. 90, no. 4, pp. 1005–1018, 2007, doi: 10.1111/j.1551-2916.2007.01515.x.

[7] I. G. Crouch, “Effects of cladding ceramic and its influence on ballistic performance,” presented at the International Symposium on Ballistics, Atlanta, GA, USA, 2014.

[8] J. E. Field, S. M. Walley, W. G. Proud, H. T. Goldrein, and C. R. Siviour, “Review of experimental techniques for high rate deformation and shock studies,” *Int. J. Impact Eng.*, vol. 30, no. 7, pp. 725–775, Aug. 2004, doi: 10.1016/j.ijimpeng.2004.03.005.

[9] W. Chen and B. Song, *Split Hopkinson (Kolsky) Bar - Design, Testing and Applications*. Springer.

[10] M. A. Meyers, *Dynamic Behavior of Materials*. John Wiley & Sons, Inc., 1994.

[11] K T Ramesh, in *Springer Handbook of Experimental Solid Mechanics*, 2008.

[12] S. Nemat-Nasser, J. B. Isaacs, and J. E. Starrett, “Hopkinson techniques for dynamic recovery experiments,” *Proc. R. Soc. Lond. Ser. Math. Phys. Sci.*, Nov. 1991, doi: 10.1098/rspa.1991.0150.

[13] R. J. Christensen, S. R. Swanson, and W. S. Brown, “Split-hopkinson-bar tests on rock under confining pressure,” *Exp. Mech.*, vol. 12, pp. 508–513, 1972, doi: https://doi.org/10.1007/BF02320747.

[14] S. Ellwood, L. J. Griffiths, and D. J. Parry, “Materials testing at high constant strain rates,” *J. Phys. [E]*, vol. 15, no. 3, p. 280, 1982.

[15] C. E. Frantz, P. S. Follansbee, and W. J. Wright, “New experimental techniques with the split Hopkinson pressure bar,” Los Alamos National Lab. (LANL), Los Alamos, NM (United States), LA-UR-83-3422; CONF-840653-1, Jan. 1984. doi: 10.2172/6854600.

[16] Q. Ping, Z. Fang, D. Ma, and H. Zhang, “Coupled Static-Dynamic Tensile Mechanical Properties and Energy Dissipation Characteristic of Limestone Specimen in SHPB Tests,” *Adv. Civ. Eng.*, pp. 1–11, 2020, doi: https://doi.org/10.1155/2020/717928.

[17] G. Ravichandran and G. Subhash, “Critical Appraisal of Limiting Strain Rates for Compression Testing of Ceramics in a Split Hopkinson Pressure Bar,” *J. Am. Ceram. Soc.*, vol. 77, no. 1, pp. 263–267, 1994, doi: 10.1111/j.1151-2916.1994.tb06987.x.

[18] I Szlufarska, K T Ramesh, and D H Warner, “Simulating Mechanical Behavior of Ceramics Under Extreme Conditions,” *Annu. Rev. Mater. Res.*, vol. 43, pp. 131–156, 2013, doi: 10.1146/annurev-matsci-071312-121714.

[19] J. Lankford, “Mechanisms Responsible for Strain-Rate-Dependent Compressive Strength in Ceramic Materials,” *J. Am. Ceram. Soc.*, vol. 64, no. 2, p. C-33-C–34, 1981, doi: 10.1111/j.1151-2916.1981.tb09570.x.

[20] H. Wang and K. T. Ramesh, “Dynamic strength and fragmentation of hot-pressed silicon carbide under uniaxial compression,” *Acta Mater.*, vol. 52, no. 2, pp. 355–367, Jan. 2004, doi: 10.1016/j.actamat.2003.09.036.

[21] S. Sarva and S. Nemat-Nasser, “Dynamic compressive strength of silicon carbide under uniaxial compression,” *Mater. Sci. Eng. A*, vol. 317, no. 1, pp. 140–144, Oct. 2001, doi: 10.1016/S0921-5093(01)01172-8.

[22] T Jiao, Yulong Li, K T Ramesh, and A A Wereszczak, “High Rate Response and Dynamic Failure of Structural Ceramics,” vol. 1, no. 3, pp. 243–253, 2004.

[23] I. M. Pickup and A. K. Barker, “Damage kinetics in silicon carbide,” *AIP Conf. Proc.*, vol. 429, no. 1, pp. 513–516, Jul. 1998, doi: 10.1063/1.55698.

[24] K. Eswar Prasad and K. T. Ramesh, “Hardness and mechanical anisotropy of hexagonal SiC single crystal polytypes,” *J. Alloys Compd.*, vol. 770, pp. 158–165, Jan. 2019, doi: 10.1016/j.jallcom.2018.08.102.

[25] P. Lundberg, L. Westerling, and B. Lundberg, “Influence of scale on the penetration of tungsten rods into steel-backed alumina targets,” *Int. J. Impact Eng.*, vol. 18, no. 4, pp. 403–416, Jun. 1996, doi: 10.1016/0734-743X(95)00049-G.

[26] M. K. Khan, M. A. Iqbal, V. Bratov, N. F. Morozov, and N. K. Gupta, “An investigation of the ballistic performance of independent ceramic target,” *Thin-Walled Struct.*, vol. 154, 2020, doi: https://doi.org/10.1016/j.tws.2020.106784.

[27] X. Quan, R. A. Clegg, M. S. Cowler, N. K. Birnbaum, and C. J. Hayhurst, “Numerical simulation of long rods impacting silicon carbide targets using JH-1 model,” *Int. J. Impact Eng.*, vol. 33, no. 1, pp. 634–644, Dec. 2006, doi: 10.1016/j.ijimpeng.2006.09.011.

[28] C. G. Fountzoulas, B. A. Cheeseman, and J. C. LaSalvia, “Simulation of Ballistic Impact of a Tungsten Carbide Sphere on a Confined Silicon Carbide Target,” Spain, Jun. 2009. Accessed: Jun. 26, 2021. [Online]. Available: https://apps.dtic.mil/sti/citations/ADA503233

[29] Z. Wang and P. Li, “Dynamic failure and fracture mechanism in alumina ceramics: Experimental observations and finite element modelling,” *Ceram. Int.*, 2015, doi: http://dx.doi.org/10.1016/j.ceramint.2015.06.110.

[30] D. Zhang, L. G. Zhao, and A. Roy, “Mechanical Behavior of Silicon Carbide Under Static and Dynamic Compression,” *J. Eng. Mater. Technol.*, vol. 141, no. 1, Jul. 2018, doi: 10.1115/1.4040591.

[31] J. Venkatesan, M. A. Iqbal, and V. Madhu, “Experimental and numerical study of the dynamic response of B4C ceramic under uniaxial compression,” *Thin-Walled Struct.*, vol. 154, p. 106785, Sep. 2020, doi: 10.1016/j.tws.2020.106785.

[32] G. R. Johnson and T. J. Holmquist, “An improved computational constitutive model for brittle materials,” *AIP Conf. Proc.*, vol. 309, no. 1, pp. 981–984, Jul. 1994, doi: 10.1063/1.46199.

[33] T. J. Holmquist, D. W. Templeton, and K. D. Bishnoi, “Constitutive modeling of aluminum nitride for large strain, high-strain rate, and high-pressure applications,” *Int. J. Impact Eng.*, vol. 25, no. 3, pp. 211–231, Mar. 2001, doi: 10.1016/S0734-743X(00)00046-4.

[34] G. R. Johnson and W. H. Cook, “A constitutive model and data for metals subjected to large strains, high strain rates and high temperatures,” 1983. doi: https://doi.org/10.1038/nrm3209.

[35] G. R. Johnson and W. H. Cook, “Fracture characteristics of three metals subjected to various strains, strain rates, temperatures and pressures,” *Eng. Fract. Mech.*, vol. 21, pp. 31–48, 1985, doi: https://doi.org/10.1016/0013-7944(85)90052-9.

[36] “ABAQUS Analysis User’s Guide.” Simulia User Assistance, 2020.

[37] “ABAQUS Theory Manual.” Simulia User Assistance, 2020.

[38] S. Acharya, S. Bysakh, V. Parameswaran, and A. Kumar Mukhopadhyay, “Deformation and failure of alumina under high strain rate compressive loading,” *Ceram. Int.*, vol. 41, no. 5, Part B, pp. 6793–6801, Jun. 2015, doi: 10.1016/j.ceramint.2015.01.126.

[39] G. Hu, K. T. Ramesh, B. Cao, and J. W. McCauley, “The compressive failure of aluminum nitride considered as a model advanced ceramic,” *J. Mech. Phys. Solids*, vol. 59, no. 5, pp. 1076–1093, May 2011, doi: 10.1016/j.jmps.2011.02.003.

[40] “ABAQUS Example Problems Guide.” Simulia User Assistance, 2020.

[41] T. J. Holmquist and G. R. Johnson, “Response of silicon carbide to high velocity impact,” *J. Appl. Phys.*, vol. 91, no. 9, pp. 5858–5866, May 2002, doi: 10.1063/1.1468903.

[42] T. J. Holmquist and G. R. Johnson, “Characterization and evaluation of silicon carbide for high-velocity impact,” *J. Appl. Phys.*, vol. 97, no. 9, p. 093502, May 2005, doi: 10.1063/1.1881798.

[43] Y. Liu, B. Li, C. Wu, L. Kong, and Y. Zheng, “Smoothed particle hydrodynamics simulation and experimental analysis of SiC ceramic grinding mechanism,” *Ceram. Int.*, vol. 44, no. 11, pp. 12194–12203, Aug. 2018, doi: 10.1016/j.ceramint.2018.03.278.

[44] G. R. Johnson and T. J. Holmquist, “Response of boron carbide subjected to large strains, high strain rates, and high pressures,” *J. Appl. Phys.*, vol. 85, no. 12, pp. 8060–8073, Jun. 1999, doi: 10.1063/1.370643.

[45] R. Y. Krashanitsa and S. Shkarayev, “Computational Study of Dynamic Response and Flow Behavior of Damaged Ceramics,” presented at the Structures, Structural Dynamics, and Materials Conferences, Austin, Texas, 2005. Accessed: Jun. 27, 2021. [Online]. Available: https://arc.aiaa.org/doi/abs/10.2514/6.2005-1847

[46] D. J. Frew, M. J. Forrestal, and W. Chen, “Pulse shaping techniques for testing brittle materials with a split hopkinson pressure bar,” *Exp. Mech.*, vol. 42, no. 1, pp. 93–106, Mar. 2002, doi: 10.1007/BF02411056.

[47] A. Chrysochoos, O. Maisonneuve, G. Martin, H. Caumon, and J. C. Chezeaux, “Plastic and dissipated work and stored energy,” *Nucl. Eng. Des.*, vol. 114, no. 3, pp. 323–333, Jun. 1989, doi: 10.1016/0029-5493(89)90110-6.

[48] H. Yang, S. K. Sinha, Y. Feng, D. B. McCallen, and B. Jeremić, “Energy dissipation analysis of elastic–plastic materials,” *Comput. Methods Appl. Mech. Eng.*, vol. 331, pp. 309–326, Apr. 2018, doi: 10.1016/j.cma.2017.11.009.

[49] R. Naghdabadi, M. J. Ashrafi, and J. Arghavani, “Experimental and numerical investigation of pulse-shaped split Hopkinson pressure bar test,” *Mater. Sci. Eng. A*, vol. 539, pp. 285–293, Mar. 2012, doi: 10.1016/j.msea.2012.01.095.

[50] G. R. Sawyer and T. F. Page, “Microstructural characterization of ‘REFEL’ (reaction-bonded) silicon carbides,” *J. Mater. Sci.*, vol. 13, no. 4, pp. 885–904, Apr. 1978, doi: 10.1007/BF00570528.

[51] J. Gong, J. Wu, and Z. Guan, “Examination of the indentation size effect in low-load vickers hardness testing of ceramics,” *J. Eur. Ceram. Soc.*, vol. 19, no. 15, pp. 2625–2631, Nov. 1999, doi: 10.1016/S0955-2219(99)00043-6.

[52] J. Wade, S. Ghosh, P. Claydon, and H. Wu, “Contact damage of silicon carbide ceramics with different grain structures measured by Hertzian and Vickers indentation,” *J. Eur. Ceram. Soc.*, vol. 35, no. 6, pp. 1725–1736, Jun. 2015, doi: 10.1016/j.jeurceramsoc.2014.12.030.

[53] X. Rao, F. Zhang, X. Luo, and F. Ding, “Characterization of hardness, elastic modulus and fracture toughness of RB-SiC ceramics at elevated temperature by Vickers test,” *Mater. Sci. Eng. A*, vol. 744, pp. 426–435, Jan. 2019, doi: 10.1016/j.msea.2018.12.044.

[54] Y. H. Zhao *et al.*, “Influence of specimen dimensions and strain measurement methods on tensile stress–strain curves,” *Mater. Sci. Eng. A*, vol. 525, no. 1, pp. 68–77, Nov. 2009, doi: 10.1016/j.msea.2009.06.031.